From $LiNiO_2$ to Li_2NiO_3: Synthesis, Structures and Electrochemical Mechanisms in Li-Rich Nickel Oxides

Matteo Bianchini,* Alexander Schiele, Simon Schweidler, Sabrina Sicolo, François Fauth, Emmanuelle Suard, Sylvio Indris, Andrey Mazilkin, Peter Nagel, Stefan Schuppler, Michael Merz, Pascal Hartmann, Torsten Brezesinski, and Jürgen Janek

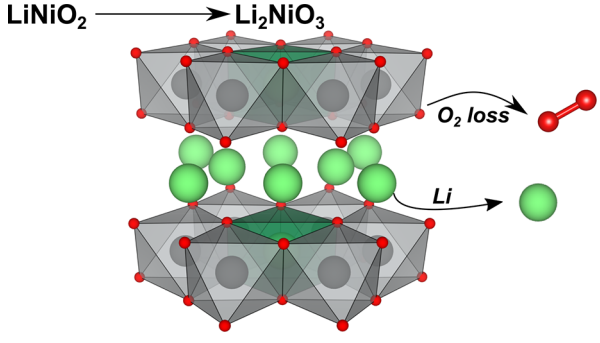

ABSTRACT: The Li−Ni−O phase diagram contains a variety of compounds, most of which are electrochemically active in Li ion batteries. Other than the well known $LiNiO_2$, here we report a facile solid state method to prepare Li_2NiO_3 and other Li rich Ni oxides of composition $Li_{1+x}Ni_{1-x}O_2$ ($0 \leq x \leq 0.33$). We characterize their crystal and electronic structure, exhibiting a highly oxidized Ni state and defects of various nature (Li−Ni disorder, stacking faults, oxygen vacancies). We then investigate the use of Li_2NiO_3 as a cathode active material and show its remarkably high specific capacity, which however fades quickly. While we demonstrate that the initial capacity is due to irreversible O_2 release, such process stops quickly in favor of more classical reversible redox mechanisms that allow cycling the material for >100 cycles. After the severe oxygen loss (~15−20%) and prolonged cycling, the Bragg reflections of Li_2NiO_3 disappear. Analysis of the diffracted intensities suggests the resulting phase is a disordered rock salt type material with high Li content, close to $Li_{0.5}Ni_{0.5}O$, never reported to date and capable of Li diffusion. Our findings demonstrate that the Li−Ni−O phase diagram has not been fully investigated yet, especially concerning the preparation of new promising materials by out of equilibrium methods.

INTRODUCTION

Positive electrode (cathode) active materials (CAMs) based on Ni and Co are thus far the primary enablers of Li ion batteries (LIBs) with high energy density.[1] Nickel, in particular, has been receiving increasing attention due to the lower cost and higher availability as compared to cobalt, making it the redox active element of choice for automotive applications, where lithium nickel−cobalt−manganese (NCM) and lithium nick el−cobalt−aluminum (NCA) oxide CAMs are employed. Today, the nickel content in both of these solid solutions may often exceed 80%, with ever increasing interest in $LiNiO_2$ (LNO), the end member of the NCM/NCA family.[2−4] Although LNO is an ideal CAM in terms of cost, specific energy, and operating voltage window, it is highly unstable in several conditions, for example, upon delithiation or heating, making its commercialization cumbersome and the use of stabilizing dopants and/or coatings indispensable.

Several phases other than LNO are present in the Li−Ni−O phase diagram, whose experimental investigation began in the 1960s.[5−11] Lithiated rock salt type oxides can be prepared with composition $Li_yNi_{1-y}O$, where typically $y < 0.3$. When increasing y, a rhombohedral layered structure forms for $0.3 < y < 0.6$ (LNO corresponds to $y = 1/2$), while for the compositions richest in Li (y up to ~2/3) a monoclinic structure has been observed. Note that the room temperature phase stability limits have been reported with some spread by different authors, so one may consider an error of ±0.02 in the y composition value [e.g., 0.30(2)]. The structures observed in the three compositional domains are closely related, since they are based on the same oxygen ccp sublattice. For low Li content, a statistical distribution of Li and Ni is observed on the cation site. For intermediate contents, Li and Ni (increasingly oxidized as y increases) order into distinct layers to minimize steric constraints, resulting in a hexagonal layered structure ($R3m$). Finally, as y further increases, a monoclinic distortion of the hexagonal lattice takes place, indicative of a layered structure with alternating Li layers and Li/Ni layers, the latter stabilized by the honeycomb ordering of the Ni and Li cations in a 2:1 ratio. The Li richest member of this solid solution, $Li_{0.67}Ni_{0.33}O$, can be written as $Li[Ni_{2/3}Li_{1/3}]O_2$, thus highlighting its relationship to LNO. However, it can also be written as Li_2NiO_3, emphasizing the isostructural nature to compounds such as Li_2MnO_3 (LMO).[12]

Li_2NiO_3 was first reported by Bronger et al.[5] and then Migeon et al.[13] Since then it has been prepared under highly oxidizing conditions by employing either a high O_2 partial pressure[5,9,13] or high mechanical pressure.[14,15] While the aforementioned synthesis methods are nonscalable and exclude any commercial relevance of Li_2NiO_3, recently a synthesis route not involving high pressure has been reported.[16,17] Although it still used large amounts of Li excess and several Li salts, requiring washing of the product made by solid state synthesis, it suggested the possibility to engineer simpler routes. Overall, this may lead to further exploitation of the compound.

The oxidation state of Ni in Li_2NiO_3 has been reported to be 4+ based on experimental results showing a diamagnetic behavior and the lowest electrical conductivity as compared to other members of the $Li_yNi_{1-y}O$ family. However, it has also been shown that the compound is prone to oxygen deficiency, expressed as $Li_2NiO_{3-\delta}$, with $\delta < 0.135$, resulting in paramagnetic behavior.[13] Hence, a fully tetravalent Ni state would be hardly reached, also consistent with the fact that $Li_2NiO_{3-\delta}$ is not completely insulating but rather behaves as a *n* type semiconductor.[13] The presence of Ni^{3+} and Ni^{4+} has also been confirmed by electron paramagnetic resonance (EPR) spectroscopy.[15] In general, it is accepted that preparing compounds with highly oxidized Ni, typically beyond 3+, is a challenging task. The synthesis of LNO itself is complex due to the highly oxidizing conditions required.[2] Tetravalent Ni occurs only in a few compounds, often in conjunction with the presence of large cations (e.g., $BaNiO_3$, $PrNiO_3$, $KNiIO_6$), and even then the actual existence of Ni^{4+} is put in doubt by spectroscopic studies, highlighting a high degree of hybrid ization of Ni and O orbitals, hence suggesting an oxidation state lower than 4+ for Ni, compensated by O^{n-} anions with $1 < n < 2$.[18−21]

As previously mentioned, Li_2NiO_3 is isostructural to Li_2MnO_3 (LMO), a well known compound of high relevance for CAMs, believed to be an inactive but stabilizing building unit in Li and Mn rich phases related to, e.g., composition $Li_{1.2}Mn_{0.54}Co_{0.13}Ni_{0.13}O_2$.[22−25] The body of literature on Li rich NCM is extensive, and some reviews can be found in refs 26 and 27. LMO itself has been attentively investigated due to the aforementioned reason and the fact that it can be easily synthesized since 4+ is a favorable oxidation state for Mn in octahedral coordination. Li removal from LMO has been demonstrated by chemical and electrochemical methods,[28,29] leading not only to high specific capacity in LIBs but also to poor reversibility. The redox mechanism is being discussed controversially in the literature.[30,31] It has recently been demonstrated using X ray absorption near edge structure (XANES), resonant inelastic X ray scattering (RIXS), and differential electrochemical mass spectrometry (DEMS) that Li deintercalation in the first charge is not compensated by Mn oxidation beyond 4+ nor by reversible O redox within the solid bulk. Instead, it is mostly irreversible O_2 (and partly CO_2) release accounting for the great majority of the capacity observed in LMO.[32−34] As a consequence, cycling Li_2MnO_3 results in significant degradation of the crystal structure.[35]

Here, we show that it is possible to prepare Li_2NiO_3 by a simple solid state route and characterize its crystal and electronic structure. We also highlight the relationship to other phases along the $LiNiO_2$−Li_2NiO_3 line. Furthermore, we use Li_2NiO_3 as CAM and investigate the redox mechanism leading to its electrochemical activity. Finally, we examine the structural stability upon cycling and reveal its evolution toward what is likely a disordered rock salt structure with high Li/Ni ratio, never reported to date.

METHODS

Synthesis. For solid state synthesis of $Li_{1+x}Ni_{1-x}O_2$ (x = 0, 0.1, 0.2, 0.33), $Ni(OH)_2$ and $LiOH{\cdot}H_2O$ (BASF SE) precursors were mixed in stoichiometric amounts $(1 - x)/(1 + x)$ and then preheated at 300 °C for 12 h. The resulting mixture was recovered and further calcined under O_2 flow at 550 °C for 12 h. The heating and cooling rates were set to 3 °C/min. The obtained powders were sieved and stored under Ar atmosphere. For the x = 0.33 sample (Li_2NiO_3), calcination at 550 °C was repeated a second time to reduce the amount of Li_2O impurities.

Electron Microscopy. Scanning electron microscopy (SEM) at different magnifications was performed at 10 kV on a LEO 1530 electron microscope (Carl Zeiss AG). Transmission electron microscopy (TEM) was performed on an FEI Titan 80 300 Cs image corrected microscope operated at 300 kV. Samples for TEM investigation were prepared using a FEI STRATA dual beam focused ion beam (FIB)/scanning electron microscope. The FIB lift out samples were milled using a Ga ion beam at 30 kV followed by final milling at 2 kV to improve the surface quality. High resolution scanning TEM (STEM) images were acquired using a high angle annular dark field (HAADF) detector (Z contrast). Indexing of the fast Fourier transform (FFT) patterns was done using the JEMS electron microscopy software package.

Diffraction. The synchrotron X ray powder diffraction (XRPD) experiments were carried out on the MSPD beamline of the ALBA synchrotron.[36] Diffraction data were collected using the one dimensional silicon based position sensitive detector MYTHEN in Debye−Scherrer geometry in a 2θ angular range of 2−55° (d range 0.7−15 Å). The wavelength was set to λ = 0.6194 Å, calibrated using a Si NIST standard. Samples were placed in quartz capillaries of 0.7 mm diameter, and the acquisition time was 5 min for all XRPD experiments. The instrumental contribution to the peak broadening was determined by measuring a $Na_2Ca_3Al_2F_{14}$ (NAC) sample. Neutron powder diffraction (NPD) was carried out on the D2B neutron diffractometer at the Institut Laue Langevin (ILL). Powder samples were put into cylindrical vanadium cans and measured in transmission geometry at λ = 1.594 Å (calibrated using NAC as reference). The data collected under these conditions were used for Rietveld structural refinements of the involved crystalline phases by means of the FullProf software.[37,38] First, a combined refinement of the XRPD and NPD data was carried out (with relative weights of 70% NPD:30% XPRD). Then the resulting parameters were used as input for Rietveld refinement including the effect of stacking faults using the FAULTS software.[39]

Electronic Conductivity. $LiNiO_2$ and Li_2NiO_3 were used to determine the respective electronic conductivity. About 200 mg of each powder was pressed (3 tons) in pellets of 1 cm diameter and ∼0.08 cm thickness (measured with a slide caliper). The electronic conductivity of the pellets was measured in custom made cells under a load of 2 tons by applying a voltage of 10 mV and recording the resulting current.

Electrochemistry. Cathodes were prepared by slurry casting onto Al foil. The slurry was obtained by dispersing 80 wt % CAM, 10 wt % Super C65 carbon black (Timcal), and 10 wt % Solef polyvinylidene fluoride binder (Solvay) in *N* methyl 2 pyrrolidone. For electro chemical testing, coin half cells consisting of cathode (3−4 mg_{CAM}/cm^2), GF/A glass microfiber separator (GE Healthcare Life Sciences), and Li metal anode (Albemarle Germany GmbH) with diameters of 13, 17, and 15 mm, respectively, using LP57 electrolyte (1 M $LiPF_6$ in 3:7 by weight ethylene carbonate and ethyl methyl carbonate; BASF SE) were assembled inside an Ar filled glovebox. All voltages are henceforth referred to Li^+/Li. Galvanostatic cycling was performed in the voltage range between 2.0 and 4.8 V at C/25 (1C = 225 mA/g) in the first 20 cycles. Subsequently, the cells were cycled at charge and

Table 1. Structural Parameters Obtained from Combined (Simultaneous) Rietveld Refinement of Synchrotron XRPD and NPD Data[a]

		χ^2 = 28.6					
$Li_2NiO_{3-\delta}$		XRPD		NPD			
S.G.: *C2/m*, *Z* = 4		R_{Bragg} = 11.8%		R_{Bragg} = 8.34%			
a = 4.9097(3) Å		R_{wp} = 26.9%		R_{wp} = 19.4%			
b = 8.4643(5) Å							
c = 4.9781(4) Å							
β = 109.226(6)°							
V = 195.34(2) Å^3							
		atomic position					
atoms	Wyckoff position	*x/a*	*y/b*	*z/c*	B_{iso}	Occ	Occ (FAULTS)
Ni	4g	0	0.168(1)	0	0.37(8)	0.78(2)	0.85(1)
Li_{Ni}	4g	0	0.168(1)	0	0.37(8)	0.22(2)	0.15(1)
Li	2b	0	0.5	0	0.5(4)	0.59(2)	0.75(1)
Ni_{Li}	2b	0	0.5	0	0.5(4)	0.41(2)	0.25(1)
Li	2c	0	0	0.5	0.9(5)	1.00(1)	1.00( )
Ni_{Li}	2c	0	0	0.5	0.9 (5)	0.00(1)	0.00( )
Li	4h	0	0.686(7)	0.5	0.9 (5)	0.98(2)	0.98( )
Ni_{Li}	4h	0	0.686(7)	0.5	0.9 (5)	0.02(2)	0.02( )
O	4i	0.225(6)	0	0.219(6)	0.7(2)	0.90(4)	0.90( )
O	8j	0.249(4)	0.316(2)	0.225(3)	0.7(2)	1( )	1( )

[a]Cation sites were constrained to be full while allowing for Ni/Li disorder. Oxygen sites were allowed for occupancy (Occ) < 1. Isotropic Debye−Waller factors (B_{iso}) were set equal between the 4i and the 8j O sites and between the 2c and the 4h Li sites to limit the number of free parameters. Stacking faults were not included, hence limiting the goodness of fit; however, one column indicating the site occupancies after the FAULTS refinement is reported (full details about the FAULTS refinement is found in the Supplementary Information).

discharge rates of *C*/5. Different lower cutoff voltages of 1.5 and 2.2 V were also tested.

Ex Situ Samples. For the preparation of ex situ samples, cathodes were cycled to different cutoff voltages (4.4, 4.65, 4.8, 3.3, and 2.2 V for Li_2NiO_3 and 4.3 V for $LiNiO_2$ to prepare $Li_{0.1}NiO_2$). A potentiostatic step was applied for 12 h at the desired voltage. Afterward, the coin cells were disassembled in an Ar filled glovebox. The cathodes were rinsed with diethyl carbonate (DEC) and dried in a vacuum at 100 °C overnight. Finally, the samples were either measured as prepared (tapes onto Al foil) or as powders (scratched off the Al foil).

X-ray Absorption Spectroscopy (XAS). The experiments were carried out at the soft X ray beamline WERA (operated by the Institute of Solid State Physics) of the Karlsruhe synchrotron light source KARA. The ex situ samples were transported to the beamline within a vacuum transfer system without exposure to air. The Ni L edge and the O K edge were measured with energy resolutions of ∼0.5 and ∼0.19 eV, respectively. Total electron yield (TEY) and partial fluorescence yield (PFY) were collected simultaneously in both cases. Data analysis included energy calibration using a NiO reference, dark signal subtraction, division by I_0, and data normalization, as previously described.[40,41]

Pressure Analysis and Differential Electrochemical Mass Spectrometry (DEMS). In situ analysis of the pressure evolution in (constant volume) custom cells was carried out as described elsewhere.[42,43] Pressure sensors (PAA33X V 3, Omega) were connected to cells with CAM (30 mm diameter with a 4 mm hole for gas extraction, 3.3 mg_{CAM}/cm^2), GF/A glass microfiber separator (36 mm diameter), Li metal anode (35 mm diameter, 600 μm thickness), and LP57 electrolyte (400 μL). For in situ gas analysis, DEMS was utilized. DEMS cells have two connections (gas in and outlets) with a special design of the upper current collector. Details are provided elsewhere.[44,45] During the measurement, a constant carrier gas flow (2.5 mL_{He}/min, purity 6.0) was used for gas extraction, and the evolved gases were analyzed by a mass spectrometer (GSD 320, OmniStar Gas Analysis System, Pfeiffer Vacuum GmbH). Li_2NiO_3, GF/A, Li metal, and LP57 were used as cathode, separator, anode, and electrolyte, respectively, as described above. The cells for both DEMS and pressure measurements were assembled inside an Ar filled glovebox.

Chemical Analysis. The metal elements were determined by inductively coupled plasma optical emission spectroscopy (ICP OES, iCAP 7600DUO from ThermoFisher Scientific). About 10 mg of the samples (weighing accuracy ±0.05 mg) was dissolved in 6 mL of hydrochloric acid and 2 mL of nitric acid at 353 K for 4 h in a graphite oven. All samples were dissolved three times. The digestions were diluted, and analysis of the elements was accomplished with 4 different calibration solutions and an internal standard (Sc). The range of the calibration solutions did not exceed a decade. Two or three wavelengths of elements were used for calculation. The oxygen content was analyzed with the method of carrier gas hot extraction (CGHE) using a commercial oxygen/nitrogen analyzer TC600 (LECO). The oxygen concentration was calibrated with the certified standard KED 1025, a steel powder from ALPHA. The calibration was verified with a commercial powder (NCM from Sigma Aldrich). The calibration range was close to the concentration of the samples. The standards and samples were weighed with a mass in the range from 1 to 2 mg (weighing accuracy ±0.05 mg) together with 5 mg of graphite in Sn crucibles (9−10 mm) and wrapped. Together with a Sn pellet (∼200 mg), the wrapped samples were put into a Ni crucible. The package was loaded in an outgassed (6300 W) double graphite crucible. The measurements took place at 5800 W. The evolving gases CO_2 and CO were swept out by helium as inert carrier gas and measured by infrared detectors.

^{7}Li Magic-Angle Spinning (MAS) Nuclear Magnetic Resonance (NMR) Spectroscopy. ^{7}Li MAS NMR spectra were measured with a Bruker Avance 200 MHz spectrometer at a magnetic field of 4.7 T, corresponding to a Larmor frequency of 77.8 MHz. Spinning was performed in 1.3 mm rotors at 60 kHz. Spectra were acquired with a rotor synchronized Hahn echo pulse sequence, a $\pi/2$ pulse length of 1 μs, and a recycle delay of 1 s. The NMR shifts are referenced to a 1 M LiCl solution at 0 ppm. The intensities are normalized with respect to the number of scans and the sample mass.

Ab Initio Simulations. Spin polarized calculations in the framework of DFT have been performed using the Vienna Ab initio Simulation Package (VASP)[46,47] with projector augmented wave pseudopotentials.[48,49] The exchange correlation functional of choice

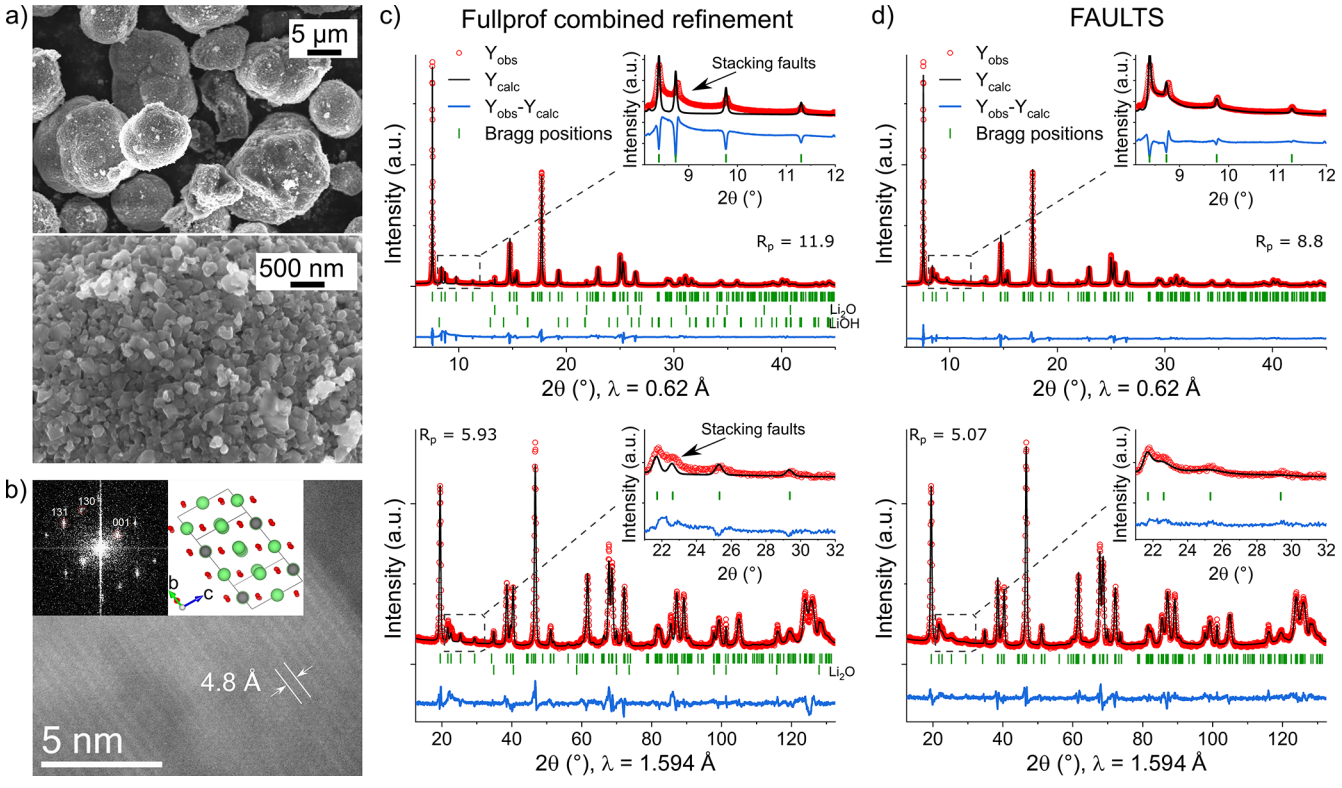

Figure 1. (a) SEM and (b) high resolution HAADF STEM images of Li_2NiO_3. (Inset in b) Fast Fourier transform (FFT) pattern. Reflections are indexed in the $C2/m$ space group, also shown in the inset. Gray spheres represent Ni, green ones lithium, and red ones oxygen. Sample's normal direction is parallel to the [−310] crystal direction. (c) Synchrotron XRPD (top) and NPD data (bottom) of Li_2NiO_3 and related combined Rietveld refinements performed with FullProf. Green ticks indicate the angular position of Bragg reflections. Red circles show the experimental diffraction pattern, black lines the calculated one from refinement, and blue lines their difference. Insets show the selected angular domain affected by stacking faults. (d) Rietveld refinements performed separately on the same XRPD/NPD data sets as in c but using the software FAULTS. Stacking faults are described with the model shown in Figure 2c.

is the strongly constrained and appropriately normed (SCAN) meta generalized gradient approximation supplemented with the long range van der Waals interaction from rVV10, the revised Vydrov van Voorhis nonlocal correlation functional, which is appropriate for layered compounds.[50] All structures have been fully relaxed with a cutoff energy of 600 eV and a k point spacing of 0.25 $Å^{-1}$ until the forces were lower than 10^{-2} eV·$Å^{-1}$. Because VASP cannot handle partial occupancies, structures with integer occupancies compatible with the experimental site occupancy factors have been generated with the combinatorial approach implemented in the supercell software.[51] The structural parameters presented in Table 1 have been fed to the software as input for creation of structural models featuring oxygen deficiency and cation disorder compatibly with the synthesized compound. With a 1 × 1 × 2 supercell, the approximate site occupancies are presented in Table S1. Even with this relatively small supercell, the number of possible combinations is 15 288 000 (reduced to 487 368 after applying symmetry operators). The software applies a point charge model to evaluate the relative stability of the structural candidates and sorts them accordingly. The cation disordered and/or oxygen deficient structures have been chosen from the most stable candidates generated with this latter step.

RESULTS

Morphology, Crystal Structure, and Stacking Faults in Li_2NiO_3. Li_2NiO_3 was synthesized by a facile solid state route from hydroxide precursors, as detailed in the Methods. Since Li_2NiO_3 requires highly oxidizing conditions to be prepared, a low annealing temperature (550 °C) was selected in order to maintain a high oxygen chemical potential μ_{O2} (the dependence of μ_{O2} on T can be expressed as

$$\mu_{O_2}(T, p_0) = \mu_0(T, p_0) + kT \ln\left(\frac{p_{O2}}{p_0}\right)$$
$$= h_0(T, p_0) - s_{O_2}T + kT \ln\left(\frac{p_{O2}}{p_0}\right)$$

[52]). To the best of our knowledge, this is the first time a simple (and potentially scalable) calcination from reactive hydroxide precursors is used to produce such Li rich nickel oxides, as opposed to previously reported syntheses routes.[5,13−17] The morphology of the Li_2NiO_3 sample from SEM and TEM imaging is shown in Figure 1a and 1b, respectively. The sample is composed of large secondary particles (5−20 μm), resulting from the agglomeration of ∼100 nm crystallites. Such a morphology is desirable for LIB applications and mostly derives from the morphology of the Ni precursor. However, the primary particle size appears smaller than typical for LIB CAMs, as a result of the higher annealing temperatures used for NCM/NCA and even LNO (≥700 °C).

The crystal structure of Li_2NiO_3 has been previously reported and found to be isostructural to Li_2MnO_3.[5] The compound has a layered structure, as can be identified by HAADF STEM (Figure 1b), where lattice fringes with spacing ≈ 4.8 Å are clearly visible. These correspond to the position of $Ni_{2/3}Li_{1/3}$ layers, while the layers of Li give little contrast, as expected by its low Z value. Li_2NiO_3 crystallizes in the monoclinic space group $C2/m$ (although it should be mentioned that it had been initially assigned to the $C2/c$ space group using a two times larger unit cell).[13,53] Alternating

Li and $Ni_{2/3}Li_{1/3}$ layers are embedded within a nearly cubic close packed oxygen sublattice (see Figure 2). In this respect,

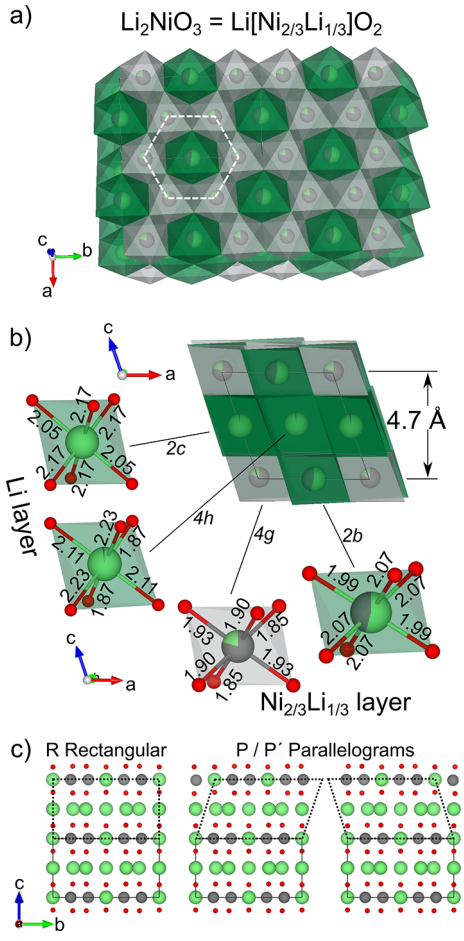

Figure 2. Crystal structure of Li_2NiO_3 viewed from different directions, as obtained from refinement of diffraction data. (a) View of the $Ni_{2/3}Li_{1/3}$ layer with honeycomb ordering highlighted (white dashed hexagon). Green spheres/octahedra represent Li and its coordination, while gray spheres/octahedra represent Ni and its coordination. Partially colored spheres represent the disorder on a given site. (b) View of Li and $Ni_{2/3}Li_{1/3}$ layers. Oxygen is at the octahedral corners (only shown in the isolated octahedra as red spheres). Ni–O and Li–O bond lengths are given in units of Angstroms. (c) Structural deviations arising from stacking faults related with cationic order. Notation is adopted from refs 62 and 63.

the relationship between Li_2NiO_3 and $LiNiO_2$ is clear, the latter being built by alternating Li and Ni layers in an analogous anion sublattice. Within the $Ni_{2/3}Li_{1/3}$ layers, steric constraints and Coulombic repulsion are minimized by a honeycomb ordering of large Li^+ cations surrounded by smaller Ni cations (~1:2 ratio, Figure 2a). To verify the structure of our sample, both synchrotron X ray and neutron powder diffraction (XRPD and NPD) experiments were performed. The observed Bragg reflections match well the expected ones (ICSD 153094[15]). The two data sets were analyzed by combined Rietveld refinement (Figure 1c). In general, the combined approach allows for refinement of more parameters simultaneously, leveraging the strength of synchrotron radiation (angular position of Bragg reflections, heavy elements) and neutrons (sensitivity to O, Li, and Debye–Waller factors).[54] The obtained structural parameters are gathered in Table 1, while the resulting crystal structure is displayed in Figure 2.

One may note from the narrow Bragg reflections that despite the low synthesis temperature, Li_2NiO_3 is well crystallized. The primary particles size, or rather the size of the coherent diffracting domains, is determined from XRPD to be 102(1) nm. This is in contrast to the fact that LNO made at the same temperature has smaller crystallites (broader Bragg reflections) and several structural defects,[55] as also discussed later in the text. The unit cell volume is 195.34 $Å^3$, i.e., in good agreement with values reported in the literature (albeit slightly larger). We also note the presence of a small amount of Li_2O and LiOH impurities, both estimated at 2.5(1) wt % from refinement. Inspection of the diffraction patterns reveals the typical superstructure peaks due to honeycomb ordering, as can be seen in the inset of Figure 1c (8–12° at 0.62 Å). However, these peaks are broad and highly asymmetric (Warren fall[56]). This suggests the presence of stacking faults, which is not surprising, as such defects have been reported for Li_2MnO_3.[39,57,58] In LMO, samples annealed at lower temperatures exhibit smaller particles size and larger amount of defects (stacking faults, vacancies, Li–Mn disorder), as shown by XRPD, NMR, and TEM.[32,57−61] Stacking fault defects are not considered in "standard" refinement programs and hence negatively affect the Rietveld goodness of fit parameters (Table 1), especially for synchrotron data, where the high angular resolution enhances the lack of proper peak shape fitting.

While the combined Rietveld refinement is nonetheless satisfactory especially thanks to the NPD data, which present intrinsically broader Bragg reflections, the effect of stacking faults was studied using the FAULTS software (Figure 1d). In particular, the typical stacking faults observed in LMO and $Li_{1+x}M_{1-x}O_2$ materials were considered, namely, a ±1/3 displacement along the *b* axis in the *C*2/*m* unit cell, causing a misalignment of the honeycomb structures along the *c* axis.[62,63] Figure 2c exhibits the regular stacking (R, rectangular) and the two possible faulted structures (P/P′, parallelogram). Details about the FAULTS refinement procedure and all relative results are given in the Supporting Information (Supplementary note 1 and Tables S2 and S3).

On the basis of "standard" combined refinement of synchrotron XRPD and NPD data, we derive the average local environments for the NiO_6 and the three LiO_6 octahedra (Figure 2b) as well as a cationic stoichiometry $[Li_{0.33}]_{2c}[Li_{0.66}Ni_{0.01}]_{4h}[Ni_{0.52}Li_{0.15}]_{4g}[Li_{0.20}Ni_{0.13}]_{2b}$. Although the obtained stoichiometry is close to the expected one, significant site disorder is found, i.e., Ni/Li mixing in three out of four crystallographic sites (Table 1). One may notice that a similar low amount of off stoichiometry (Ni in the Li layer) is present in our sample as there is typically in LNO (~1%, here in 2*c* + 4*h* sites). However, most of the mixing occurs between the 4*g* and the 2*b* sites, indicating an imperfect honeycomb ordering. To some extent this is expected due to the low annealing temperature we employed and in analogy to Li_2MnO_3.[57,61,64] On the other hand, stacking faults are directly related to the Ni/Li mixing on the 4*g* and 2*b* sites, and in fact, the most significant difference we find between a "standard" Rietveld refinement and the FAULTS refinement is in the 4*g* and 2*b* site occupancies: the Ni/Li intermixing is artificially increased when neglecting stacking faults (see Table 1), while taking them properly into account decreases it. Finally, based on the more accurate XRPD data, the FAULTS refinement yields an average cationic stoichiometry

$[Li_{0.33}]_{2c}[Li_{0.66}Ni_{0.01}]_{4h}[Ni_{0.57}Li_{0.10}]_{4g}[Li_{0.25}Ni_{0.08}]_{2b}$ on top of which a degree of stacking defects of 20% was found (as defined in the Supplementary Information). Interestingly, this compares well with the value found for LMO made from rock salt type MnO at 700 °C.[62]

We also verified the Li, Ni, and O content of the material by chemical analysis (ICP OES and CGHE, see Table 2), from which one derives $Li_{1.27(3)}Ni_{2/3}O_{1.9(2)}$, in good agreement with the refinement results. In addition to ICP OES, CGHE was used to probe the O content. The resulting data suggest the presence of O deficiency, as seen in the formula unit reported above. This fact is not surprising given the poor stability of highly oxidized Ni, and indeed, it has already been reported in the literature.[13] We also confirm the data by refinement of the oxygen site occupancies (Table 1) and ultimately obtain a stoichiometry of $[Li_{0.99}Ni_{0.01}]_{Li\_layer}[Ni_{0.65}Li_{0.35}]_{Ni\_layer}O_{1.9(1)}$ (= $Li_{1.34(5)}Ni_{0.66(5)}O_{1.9(1)}$). Interestingly, only one of the two oxygen crystallographic sites is found to be O deficient (4*i*), while the other one (8*j*) is full and hence its site occupancy fixed afterward. The reason for this behavior is not evident, as the two O sites are nearly equivalent in terms of neighboring atoms. However, distributing O vacancies on a single O site allows one to maximize the vacancy−vacancy distance, which may likely be energetically favorable.

Table 2. ICP OES and CGHE Results for Different $Li_{1+x}Ni_{1-x}O_2$ Samples[a]

x in $Li_{1+x}Ni_{1-x}O_2$	Li	Ni	O
0	1.04(2)	1.00(1)	2.00(20)
0.1	1.12(2)	0.9(1)	2.00(19)
0.2	1.21(3)	0.8(1)	2.04(20)
0.33	1.27(3)	0.67(1)	1.87(21)

[a]The techniques yield the elemental ratios of Li, Ni, and O, which were then normalized to the Ni content $(1 - x)$.

Electronic Structure of $Li_2NiO_{3-\delta}$. The structural analysis carried out so far suggests the presence of Ni in a highly oxidized state in $Li_2NiO_{3-\delta}$ based on a simple ionic bonding picture and on steric arguments according to which the honeycomb ordering is promoted by a 1:2 ratio of small to large cations ($Ni^{3/4+}$:Li^+) within a layer. This is typically the case in compounds such as $Li_2M^{4+}O_3$ with M^{4+} = Mn, Ti, Pd,

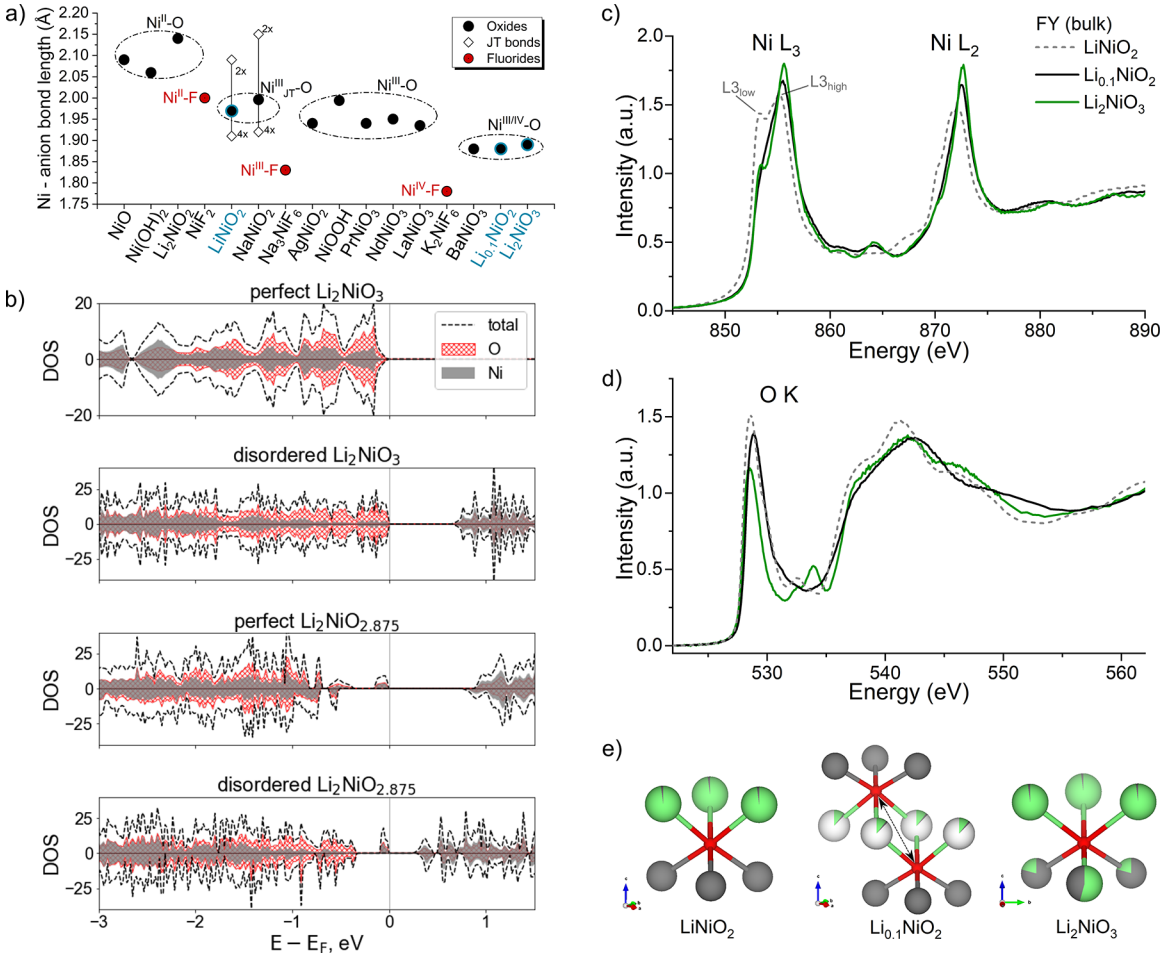

Figure 3. (a) Collection of Ni−O and Ni−F bond lengths for Ni in octahedral environment gathered from the literature and from this work (in blue: $LiNiO_2$, $Li_{0.1}NiO_2$, Li_2NiO_3). Data sources (ICSD codes and journal articles) are provided in Table S4. (b) Total and partial electronic densities of states (DOS) for perfect and cation disordered Li_2NiO_3, oxygen deficient Li_2NiO_3 ($Li_2NiO_{2.875}$), and cation disordered $Li_2NiO_{2.875}$. (c and d) Soft XAS spectra of $LiNiO_2$ (dashed gray line), $Li_{0.1}NiO_2$ (black line, ex situ sample made electrochemically from $LiNiO_2$ as described in the Methods section), and $Li_2NiO_{3-\delta}$ (green line). (c) Ni L_3 and L_2 edge spectra detected in fluorescence yield. All spectra are normalized in the same way, as described in the Methods section. (d) O K edge spectra detected in fluorescence yield. (e) Local coordination of oxygen in the three compounds. Red spheres represent oxygen, gray ones Ni, and green ones Li.

Pt, Ru, Rh, Ir, Sn. A comparative analysis of the Ni−O bond lengths found in this work with several others reported in the literature is provided in Figure 3a, gathering an overview of Ni−O and Ni−F bonds in binary and ternary compounds. It can be seen how the bond lengths decrease with increasing Ni oxidation state and that the Ni−F distances are significantly shorter than the Ni−O ones. Moreover, the bond length difference between Ni^{2+}−F and Ni^{3+}−F appears to be much larger than the difference between Ni^{3+}−F and Ni^{4+}−F as a consequence of the ionic size of Ni in its different valence states ($r(Ni^{2+})$ = 0.69 Å, $r(Ni^{3+}{}_{LS})$ = 0.56 Å, $r(Ni^{4+}{}_{LS})$ = 0.48 Å).[65] A similar tendency can be observed for the oxides, although less pronounced because of the lower ionic nature of the Ni−O bond. For the oxides of interest to this work, note that in the structure of $Li_2NiO_{3-\delta}$ (as obtained from Table 1 and in good agreement with the literature) the average Ni−O bond length is very similar to what is observed for delithiated $LiNiO_2$ ($Li_{0.1}NiO_2$) or $BaNiO_3$, the latter of which is sometimes cited as containing Ni^{4+}, but it most likely features a mixed $Ni^{3/4+}$ state, compensated by O^{n-} with $1 < n < 2$.[18] To the best of our knowledge, Ni−O bonds of 1.88 ± 0.01 Å are the shortest reported in the literature and likely indicate the presence of some amount of Ni^{4+}.

Given the presence of oxygen vacancies and structural disorder and ultimately the unclear oxidation state of Ni in $Li_2NiO_{3-\delta}$, the local electronic structure of the material was investigated in more detail by density functional theory (DFT) and soft X ray absorption spectroscopy (XAS). Later in the paper, we will expand such results by combining synchrotron XRPD and NMR spectroscopy in a series of samples $Li_{1+x}Ni_{1-x}O_2$ (x = 0, 0.1, 0.2, 0.33), representing compositions of theoretically increasing Ni oxidation state between $LiNiO_2$ and Li_2NiO_3.

We performed calculations in the DFT framework to compare the electronic properties of perfect and cation disordered Li_2NiO_3 (with Li/Ni mixing on the 4*g* and 2*b* sites similar to Table 1) and their respective oxygen vacant counterparts ($Li_2NiO_{2.875}$) and disentangled the effect of oxygen deficiency and cation disorder. While the structure of stoichiometric, perfectly ordered Li_2NiO_3 is univocal, in DFT its cation disordered and oxygen vacant variations are not; hence, their structures have been chosen from the most stable candidates generated from the supercell software as described in the Methods. Figure 3b shows the calculated electronic densities of states (DOS) of perfect Li_2NiO_3 compared to cation disordered Li_2NiO_3, $Li_2NiO_{2.875}$, and cation disordered $Li_2NiO_{2.875}$. Perfect Li_2NiO_3 exhibits a wide band gap, higher than 1.5 eV even at the DFT level that notoriously underestimates it. The spin resolved DOS is also perfectly symmetric, and no spin population is found on any Ni atom (Table S5), consistent with the presence of Ni^{4+} and with the diamagnetic properties and low electrical conductivity, as indeed reported in the literature.[13] Cation disorder in stoichiometric Li_2NiO_3 reduces sensibly the band gap but does not change the magnetic behavior, as evidenced by the symmetric DOS. The effect of oxygen deficiency is more noteworthy. The spin up and spin down DOS become asymmetric, with the spin up one displaying an extra peak close to the Fermi level. This indicates that the compound is paramagnetic and is also consistent with n type semiconducting behavior, as proven experimentally.[13] The extra peak is due to the overlap of Ni and O partial densities of states and is thought to have a strong covalent character. The spin population confirms this picture (Table S5), identifying two Ni atoms in a high spin state in the supercells carrying a lone electron (~0.76 e^-), which classifies them as Ni^{3+}. A smaller but non negligible spin (~0.2 e^-) is found on two oxygen atoms that connect to the Ni^{3+}. Here as well, cation disorder is found to have a secondary effect in modifying the DOS: the broken symmetry results in a slightly higher spin population on two Ni (~0.80 e^-) complemented by ~0.15 e^- on one of the two oxygen atoms connecting Ni^{3+} and ~0.09 e^- on two further oxygen atoms.

Figure 3c shows the soft XAS spectrum of Li_2NiO_3 at the Ni L edges collected in fluorescence yield mode, thus representative of the material's bulk properties. For comparison, the spectrum of $LiNiO_2$ is reported (theoretically representing Ni^{3+}) as well as that of $LiNiO_2$ charged electrochemically to composition $Li_{0.1}NiO_2$ (theoretically $Ni^{3.9+}$). As previously discussed, care must be taken in assigning formal oxidation states to Ni in $LiNiO_2$ related compounds because several authors and our own DFT calculations have shown that the Ni orbitals are strongly hybridized with the O 2p ones.[66,67] However, from a qualitative standpoint, one clearly sees that $LiNiO_2$ has the expected doublet shape on the L3 edge ($L3_{high}$ at 855 eV, $L3_{low}$ at 853 eV), as often reported for the compound.[68,69] In particular, the ratio of the two peaks has been used to assign the more oxidized/more reduced character of Ni states. Typically, Ni^{2+} in NiO exhibits a single peak $L3_{low}$ (see Figure S1), while LNO features a doublet peak with $L3_{high}$ more intense than $L3_{low}$. When the sample is more reduced than it should be (for example, if a surface rock salt like region is present, as can be seen in total electron yield mode), the peak $L3_{low}$ grows in intensity with respect to the peak $L3_{high}$ (see Figure S1), i.e., more akin to NiO. Note that in Figure 3c the LNO sample has a $L3_{high}/L3_{low}$ peak ratio well beyond 1 (and beyond most recently reported values[68,69]), indicating high Ni oxidation state in our sample.

When extracting Li from LNO to reach $Li_{0.1}NiO_2$, both the L3 and the L2 edges shift toward higher energy, as expected when oxidizing Ni. The edges' shape also changes significantly with the doublet structure becoming less pronounced (again, in line with reports on charged LNO and NCM111[68,70,71]), and a new feature appears at 864 eV. Despite the very different stoichiometry, the XAS spectra of $Li_2NiO_{3-\delta}$ ($\delta \approx 0.1$) and $Li_{0.1}NiO_2$ are quite similar, which tends to indicate that the local environment around Ni and its electronic behavior are closely related. On the basis of these data, supported by the structural characterization and the DFT calculations, we suggest both spectra are representative of a highly oxidized Ni state, containing Ni^{4+} species ($3d^6$ or rather $t_{2g}{}^6e_g{}^0$ in octahedral environment) with residual Ni^{3+} ones. Nonetheless, for properly describing the Ni local electronic environment based on soft XAS data, multiplet calculations should be performed.[72] A very recent study[73] shows strong evidence that Ni L2,3 NEXAFS measurements on NCM cathode materials can be well described with a superposition of Ni^{2+} and Ni^{3+} states and, moreover, that redox reactions in NCMs proceed via reversible oxidation of Ni and a strong hybridization with O. They find that it is thus the amount of more "ionic" Ni^{2+} which can be oxidized to strongly hybridized Ni^{3+} that seems to limit the reversible capacity of the materials. Again, this evidences the complex electronic structure of such compounds, suggesting the presence of significant Ni−O orbitals hybridization.[74−76]

Figure 3d shows the XAS intensity collected in fluorescence yield mode at the O K edge. Here, differences between the spectra are clearly visible. This is to be expected since the local environment of the oxygen (see Figure 3e) is very different in $LiNiO_2$, $Li_{0.1}NiO_2$, and Li_2NiO_3. In the first case, the oxygen has 3 Ni neighbors and 3 Li neighbors; in $Li_{0.1}NiO_2$, O has 3 Ni neighbors and virtually no Li nearby. Hence, O−O interactions become also significant. Finally, Li_2NiO_3 has oxygen with 2 Ni neighbors and 4 Li neighbors on average.

In conclusion, XAS allowed us to confirm the presence of highly oxidized Ni, most likely a mixture of trivalent and tetravalent states, and to draw a parallel between deintercalated LNO ($Li_{0.1}NiO_2$) and $Li_2NiO_{3-\delta}$ with focus on the Ni electronic states rather than the oxygen ones.

$Li_{1+x}Ni_{1-x}O_2$ Solid Solution (x = 0, 0.1, 0.2, 0.33). To further understand the evolution of the hexagonal $LiNiO_2$ structure toward monoclinic $Li_{1.33}Ni_{0.67}O_2$ (Li_2NiO_3), a series of samples $Li_{1+x}Ni_{1-x}O_2$ (x = 0, 0.1, 0.2, 0.33) was prepared under otherwise identical conditions. Synchrotron XRPD data are displayed in Figure 4a. First, one notices that the crystallinity of the samples differs (as highlighted in the inset, representing the different broadening of the $003_h = 001_m$ Bragg reflections). This confirms that as the Li content increases, a lower temperature is needed to successfully prepare the materials. Here, a temperature of 550 °C was selected as optimal for synthesizing samples with x = 0.33, which results in less crystalline samples for lower x values. As displayed in the second inset, we clearly observe the appearance of superstructure peaks, characteristic of the monoclinic unit cell. While the background for LNO (x = 0) is flat in the region 8−12°, Bragg reflections are present in Li_2NiO_3, exhibiting the previously discussed peculiar broadening due to stacking faults. The same superstructure peaks but further broadened are visible for $Li_{1.2}Ni_{0.8}O_2$ (x = 0.2), suggesting a large degree of stacking defects. On the other hand, only an unstructured bump is noticed for $Li_{1.1}Ni_{0.9}O_2$ (x = 0.1), indicating that the extra Li already occupies the Ni layer in a way that is not fully random, but honeycomb like local environments (short range ordering) are already being defined. In fact, the structure of the samples x = 0 and 0.1 can be refined using a hexagonal unit cell (taking into account a strong anisotropic peak broadening, as described in the Supporting Information of ref 55 and in Figures S2 and S3 and Tables S6 and S7), while for x = 0.2 and 0.33, a monoclinic one is necessary (see Figure S4 and Table S8). This agrees with the literature, where however the nature of the hexagonal to monoclinic phase transition has not yet been clarified.[15] In Figure 4b, a comparison of the primitive cell volumes ($2V/Z$) for the different samples is presented, indicating a linear trend (Vegard's law) typical of a single solid solution for all values of x with an order−disorder phase transition (from isolated to correlated honeycombs) occurring between x = 0.1 and 0.2.

Finally, ^{7}Li MAS NMR spectroscopy experiments were carried out for samples across the $Li_{1+x}Ni_{1-x}O_2$ solid solution (see Figure 4c). The spectrum of the sample with x = 0 (LNO) is dominated by a broad peak at 719 ppm. The large NMR shift is caused by transfer of unpaired electron spin density from paramagnetic Ni^{3+} (electron configuration $3d^7$) via Ni−O−Li bonds to the Li nuclei.[77] This shift value is characteristic of $LiNiO_2$, where Li has 12 Ni^{3+} neighbors, 6 of them connected to Li via ∼180° oxygen bonds and 6 of them connected via ∼90° bonds.[78,79] A small narrow peak at 0 ppm

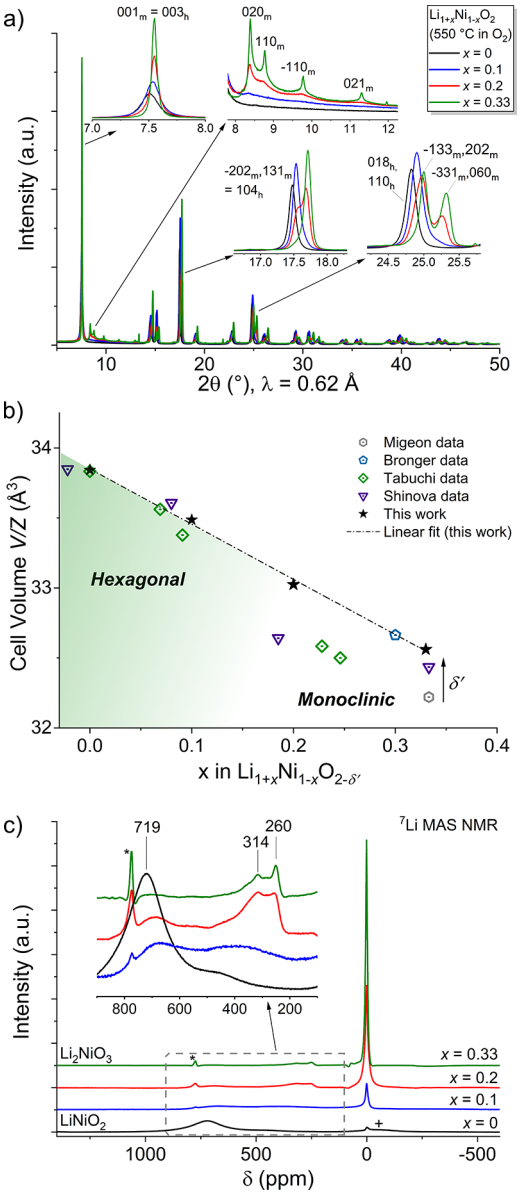

Figure 4. (a) Synchrotron XRPD of $Li_{1+x}Ni_{1-x}O_2$ (x = 0, 0.1, 0.2, 0.33) synthesized under identical conditions. Insets show selected angular domains with Bragg reflections indexed in the respective space group (h = hexagonal $R3m$, m = monoclinic $C2/m$). (b) Evolution of the normalized unit cell volume V/Z as a function of x in $Li_{1+x}Ni_{1-x}O_{2-\delta'}$. Qualitative effect of δ' on the unit cell volume is also indicated ($\delta' = 2\delta/3$). Literature data are included for comparison.[5,13,15,16] Linear fit to the data points from this work is shown. Note that for x = 0.33, Z = 6 or 4 depending on whether one writes Li_2NiO_3 or $Li_{1.33}Ni_{0.67}O_2$. (c) ^{7}Li MAS NMR spectra of $Li_{1+x}Ni_{1-x}O_2$. Spinning sidebands are marked with an asterisk and a plus sign.

likely represents a small amount of diamagnetic impurities such as LiOH or Li_2CO_3. When the Li concentration is increased, the intensity of the peak at 719 ppm is reduced and a strong peak at 0 ppm gradually appears. Furthermore, additional small peaks in the range between 200 and 400 ppm in samples with x = 0.1 and 0.2 reveal an increasing amount of Li in the Ni layers with mixed Ni^{3+}/Ni^{4+} neighbors. The very small NMR shift indicates a diamagnetic Li environment, i.e., that Li has mostly Ni^{4+} ($3d^6$) neighbors, consistent with the previous considerations. As further proof, the assignment is also supported by

the low electronic conductivity of $Li_2NiO_{3-\delta}$. From our measurements, we find σ = 2.2 mS/cm, about 40 times lower than the value measured in the same way for $LiNiO_2$ (84.2 mS/cm) but still close to those of most semiconductors (rather than insulators).

Electrochemical Behavior of $Li_{1+x}Ni_{1-x}O_2$ CAMs in LIBs. Although a simple ionic bonding picture is simplistic to describe both LNO and $Li_2NiO_{3-\delta}$, we have shown by DFT and XAS that, in a good approximation, the coordination and oxidation state of Ni in $Li_2NiO_{3-\delta}$ is equivalent to that of $Li_{0.1}NiO_2$, i.e., Ni is oxidized beyond the trivalent state. Under these circumstances, $Li_2NiO_{3-\delta}$ is supposed to be virtually electrochemically inactive when used as CAM due to the inability of the transition metal to further oxidize upon Li extraction. However, the same reasoning applies to Li_2MnO_3, which shows electrochemical activity[30] mostly due to oxygen oxidation and O_2 release from the lattice.[33] In LIBs, LMO delivers 350 mAh/g upon charge (2.0–4.8 V) via a long flat plateau around 4.5 V and 260 mAh/g upon discharge.[59] A close to theoretical specific capacity can be obtained by increasing the cutoff voltage to 5.0 V but at the expense of reversibility.[32] In general, the electrochemical behavior of LMO used as CAM is dependent on the synthesis method of choice; for example, samples annealed at lower temperatures are associated with higher electrochemical activities (because of smaller particle size).[32,57−61,64] Thus, it is important to verify the electrochemical activity of $Li_2NiO_{3-\delta}$ as CAM in LIBs. To this end, half cells were assembled and tested. The theoretical specific capacity of the material based solely on the Li availability is very high, namely, 444 mAh/g_{CAM}. If any redox chemistry exists, a potentially high capacity can be expected. Figure 5 gathers the electrochemical data.

The first cycle has indeed a high specific charge capacity approaching 300 mAh/g_{CAM}, yet Coulombic efficiency is rather poor at around 70%. Li is surely extracted from the Li layer in the crystal structure, whereas extraction of Li from the $Ni_{2/3}Li_{1/3}$ layer is at present an open question. The first cycle voltage profile exhibits a sloped character with a first small plateau around 4.5 V and a second long one occurring at 4.75 V (see Figure 5a). The overall behavior is in rather good agreement with the one observed by Tabuchi et al.[16] The first discharge and subsequent cycles are very different from the first charge, i.e., the high voltage plateau rapidly disappears. The shape of these curves is reminiscent of the voltage profiles typical of disordered rock salt CAMs.[80] These varying electrochemical profiles suggest marked and likely irreversible changes to the crystal structure of the compound already during the first charge. Nonetheless, the material can be cycled over 100 cycles (Figure 5b). The specific discharge capacity increases during the first few cycles, reaching a maximum of 238 mAh/g_{CAM}, and then starts decreasing. After 20 cycles, the Coulombic efficiency stabilizes above 99%, indicating reversible electrochemical phenomena. Yet, after 120 cycles, only a fraction of the initial capacity is retained (~100 mAh/g_{CAM}).

It should be noted that the observed capacity and electrochemical behavior are highly dependent on the choice of the cutoff voltage; most capacity in the initial charge is obtained between 4.7 and 4.8 V; thus, at least 4.8 V is needed as an upper cutoff to observe such "activation". Moreover, before the 4.75 V plateau, the voltage profile may peak at roughly 4.78 V, depending on the cell polarization (as it happens in Figure 5a but not in Figure 7), which makes the choice of the upper cutoff even more critical. Further extending

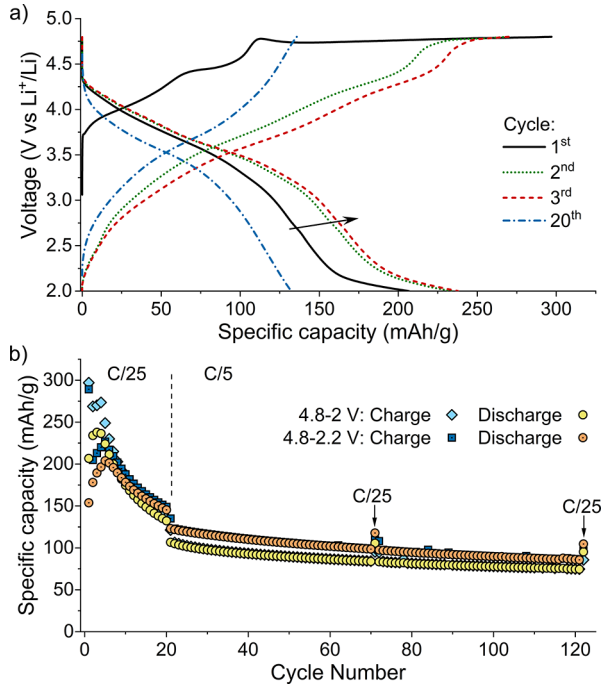

Figure 5. (a) Voltage profiles of Li_2NiO_3 half cells cycled at 25 °C and C/25 rate in the voltage range between 2.0 and 4.8 V. No potentiostatic step is used at 4.8 V. Only the first 3 cycles and the 20th cycle are shown for clarity. (b) Specific capacity as a function of cycle number for half cells cycled in the voltage window 2.0–4.8 and 2.2–4.8 V.

the upper cutoff to 5.0 V allows for higher initial charge capacity by extending the plateau's length, as in the case of LMO, but it causes severe electrolyte degradation and cell failure. The lower cutoff voltage can be set to 2.0 V, as in Figure 5a, or it can be lowered to 1.5 V, which results not only in higher specific discharge capacity but also in faster cell degradation (Figure S5). On the other hand, limiting the cutoff to 2.2 V can improve capacity retention, as shown in Figure 5b.

The samples with x = 0–0.2 have also been electrochemically tested (Figure 6). In general, all observed capacities are rather low; for example, x = 0 corresponds to $LiNiO_2$, yet the observed specific discharge capacity is only 149 mAh/g_{CAM} due to the nonideal synthesis conditions (550 °C). Within a limited voltage window (3.0–4.3 V), the observed capacity decreases with increasing x, as could be expected by the reduced amount of available Ni redox activity (notice the linear correlation between the amount of Ni^{3+} and the (dis)charge capacity in Figure 6). Increasing the voltage range to 2.0–4.8 V results, for all x, in a higher first cycle specific charge capacity due to the appearance of a plateau similar to that of Li_2NiO_3 but with little reversibility in the subsequent cycles. Furthermore, the observed discharge capacities decrease linearly with increasing x.

Charge Compensation Mechanism in Li_2NiO_3. To understand the observed capacity and the origin of the charge compensation, in situ pressure analysis and DEMS measurements were performed, allowing one to track the pressure evolution with cycling as well as to determine the nature of gaseous species evolved. Figure 7a shows the evolution of pressure inside the electrochemical cell over 5 cycles. One can clearly notice a large pressure increase during the first charge, starting from about 4.4 V, followed by a slight decrease during

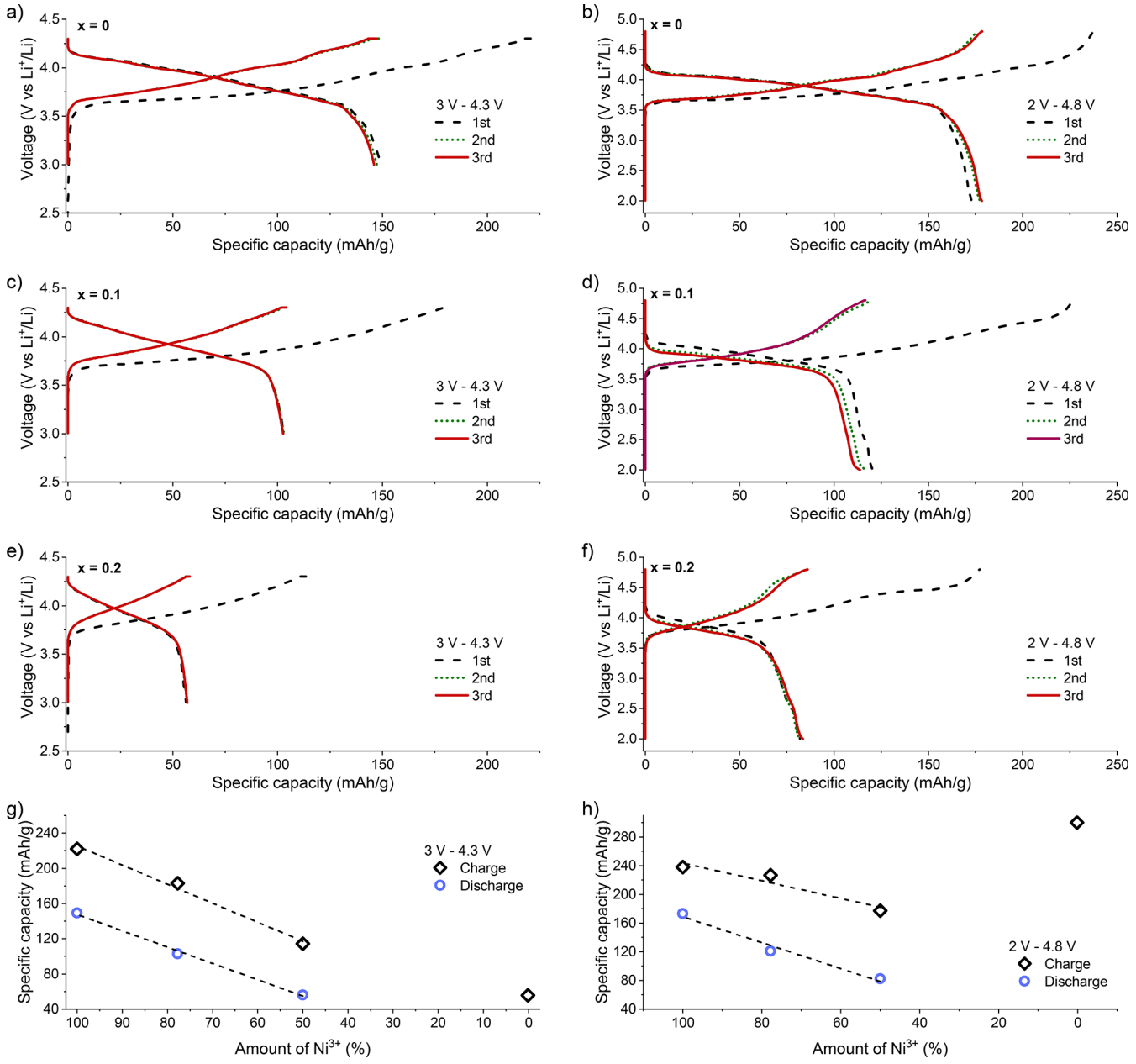

Figure 6. Voltage curves for $Li_{1+x}Ni_{1-x}O_2$ half cells ($x = 0$ (a and b), $x = 0.1$ (c and d), $x = 0.2$ (e and f)) cycled at $C/25$ rate between 3.0 and 4.3 V (a, c, e) and 2.0 and 4.8 V (b, d, f). First (dashed black), second (dotted green), and third (solid red) cycles are shown. (g and h) Specific charge and discharge capacity as a function of theoretical Ni^{3+} content in $Li_{1+x}Ni_{1-x}O_2$ ($x = 0$, 0.1, and 0.2).

the subsequent discharge. During each following charge, the pressure inside the cell increases further but by a smaller amount until nearly no increase is observed in the fifth cycle.

Using DEMS, the pressure increase can be assigned to the related gaseous species. The results in Figure 7b and 7c suggest that the first charge is dominated by O_2 loss from Li_2NiO_3, although CO_2 is also formed. Note that until 4.4 V the rate of O_2 released is small and comparable to that of $LiNiO_2$ (~40 nmol/min/g_{CAM} at 4.3 V). Beyond 4.4 V, the O_2 release increases by a factor of ~200, reaching a value comparable to that observed for Li_2MnO_3 (still about two times larger for Li_2NiO_3).[33,81] The nearly linear profile of the integrated O_2 signal ($d(n_{O2})/dt$) can be used in conjunction with the galvanostatic current (dq/dt) to obtain the amount of electrons exchanged per mole of O_2 released. We find 3.8 mol_{e^-}/mol_{O2}, confirming that the O_2 release corresponds nearly to a $4e^-$ process as expected. The same analysis cannot be directly extended to the CO_2 gas released since its behavior is rather nonlinear.

By combining the amounts of both gases and considering O_2 and CO_2 release as $4e^-$ processes, we can calculate that they should result in a specific capacity of 247 mAh/g_{CAM}, very close to the experimentally observed 254 mAh/g_{CAM}. However, one should also take into account that, in the first charge, virtually no gas evolution is observed until 4.4 V, corresponding to about 60 mAh/g_{CAM} that are not due to gas release (see Figures 5a and 7). Moreover, some of the CO_2 evolved from our sample may be due to Li_2CO_3 decom position, which is a well known source of CO_2 in Ni rich CAMs, especially during the first charge.[82] Li_2CO_3 is likely

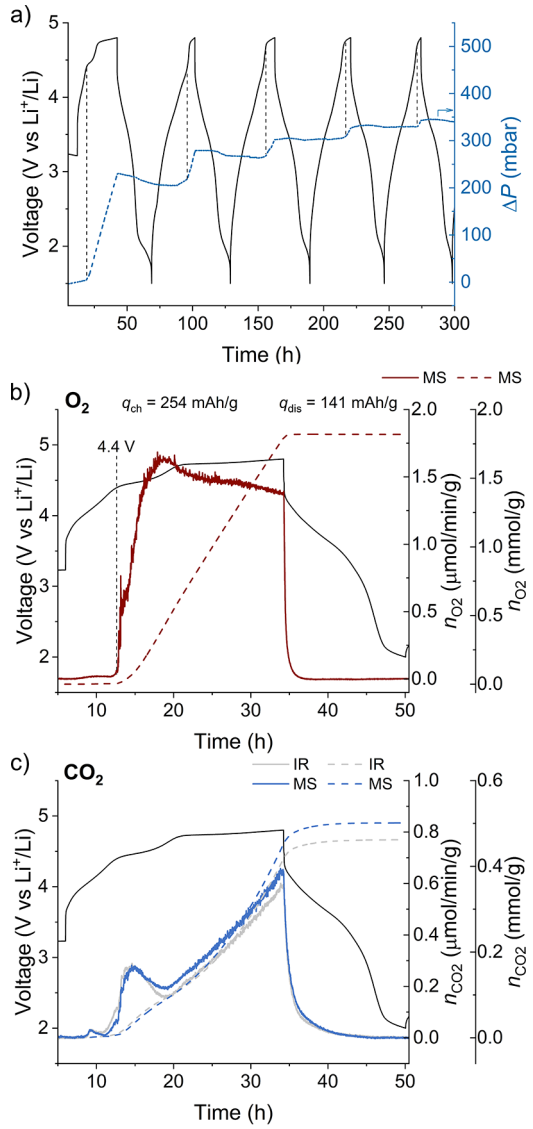

Figure 7. (a) In situ pressure analysis of a Li_2NiO_3 half cell cycled at C/25 rate and 25 °C for 5 cycles in the voltage range between 1.5 and 4.8 V. Voltage profile vs Li reference electrode (black) and corresponding pressure changes (blue). Onset of pressure increase is denoted by gray dashed lines. (b and c) First cycle gas evolution rates of O_2 and CO_2 (solid red, blue and gray lines) and cumulative amount of gas evolved (dashed red, blue and gray lines) as a function of time during DEMS measurement. Voltage curve is also shown for clarity (solid black line).

present in our sample after reaction of surface impurities with atmospheric CO_2 or the carbonate electrolyte. Thus, neglecting CO_2 results in a specific capacity of 193 mAh/g_{CAM} due to O_2 release (see Table 3 and Figure 7) plus 60 mAh/g_{CAM} due to redox mechanism(s), which matches well with the 254 mAh/g_{CAM} experimentally observed. As for the redox active elements, in $Li_{1.33}Ni_{0.67}O_{2-\delta'}$ ($\delta' = 2\delta/3$), in a simplistic ionic picture, the oxidation state of Ni would be 4−3δ'. From NPD, we estimated $\delta' = 0.1$, suggesting that some capacity may result from Ni oxidation. However, the large error bars on the actual oxygen deficiency do not allow quantitatively estimating the expected capacity. Hence, the presence of Ni redox is unclear, and an O redox mechanism is equally likely. In fact, in $LiNiO_2$, O redox is observed above 4.3 V.[83] We have also shown by DFT (Figure 3b) that in $Li_{1.33}Ni_{0.67}O_{2-\delta'}$ containing O vacancies, an extra peak of covalent character in the DOS appears near the Fermi level due to the overlap of Ni and O electronic states. We thus suggest the electrons populating such DOS peak may be responsible for the redox activity.

To verify the Ni/O redox contribution, soft XAS experiments were conducted on ex situ samples charged (i.e., electrochemically delithiated) to different upper cutoff voltages (see Figure 8a and Figure S6). The results show no signs of Ni oxidation. On the contrary, Ni appears to be slightly reduced (increasing intensity of $L3_{low}$ as compared to $L3_{high}$) during charge, even to only 4.4 V, i.e., before the onset of O_2 release. This suggests either that holding the voltage at 4.4 V during ex situ sample preparation was sufficient to induce significant oxygen release, hence partially reducing the Ni, or that O redox processes also play a role at rather low voltage, thereby inducing charge redistribution around Ni. The latter scenario appears to be supported by the O K edge XAS data, since the spectral shape is strongly altered after charge to 4.4 V. Interestingly, little change is observed on both edges upon further charging to 4.65 and 4.8 V. These results indicate that minor changes occur in the electronic structure of Ni and O in the lattice at high voltages, supporting the DEMS data in that most of the capacity comes from gas release above 4.4 V. During discharge to 3.3 and 2.0 V (see Figure 8b), the Ni (increasing $L3_{low}/L3_{high}$ ratio) and O edges are both significantly modified, which is indicative of reduction of both species. This result also suggests that the subsequent cycles increasingly rely on redox activity from the Ni.

In summary, we can conclude that the dominant charge compensation mechanism during the initial charge is O_2 release, contributing to at least 76% of the observed specific capacity. For the remaining part, a small amount of CO_2 release could be contributing if being formed as a consequence of singlet oxygen release.[84] However, based on the soft XAS data, it is likely that O redox plays a role as well, despite the fact that this has not been observed for Li_2MnO_3. This may be due to the energy levels generated by the O vacancies in the DOS near the Fermi level of $Li_{1.33}Ni_{0.67}O_{2-\delta}$. Investigating the redox activity of O in the compound will be the subject of future work.

Structure of Li_2NiO_3 after Prolonged Electrochemical Cycling. After the first few charge/discharge cycles, the large amount of O_2 loss permanently modifies the stoichiometry and oxidation state of the material, allowing for fairly stable cyclability based on standard redox processes. However, given the substantial amount of O_2 that is lost from the crystal

Table 3. Amounts of Gas Evolved during the First Cycle (from DEMS), Relative Specific Capacities ($4e^-$ processes), and Change in CAM Oxygen Content

O_2 release [mmol/g]	specific capacity (based on O_2) [mAh/g]	CO_2 release [mmol/g]	total gas (O_2 + CO_2) release [mmol/g]	total expected specific charge capacity [mAh/g]	experimental specific charge capacity [mAh/g]	k after O_2 loss (Li_2NiO_k)	k after O_2 + CO_2 loss (Li_2NiO_k)
1.8	193	0.5	2.3	247	254	2.56	2.44

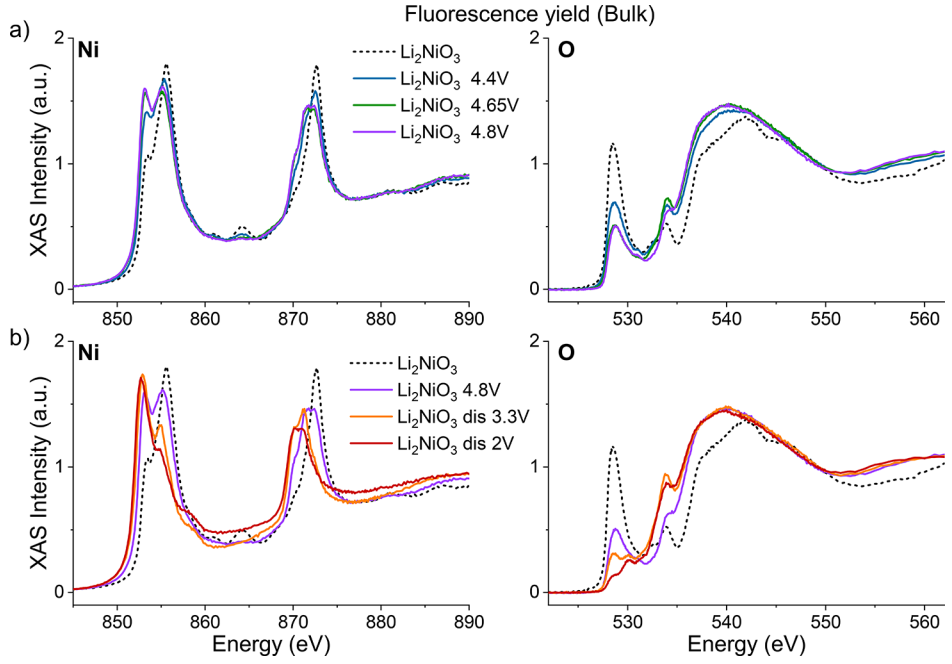

Figure 8. Soft XAS spectra in fluorescence yield of Li_2NiO_3 prepared ex situ by charge or discharge to different voltages. Pristine Li_2NiO_3 is shown as reference as a dashed black line. All spectra are normalized in the same way, as described in the Methods section. Ni L_3 and L_2 edge spectra (left) and O K edge spectra (right). (a) Charged to 4.4, 4.65, and 4.8 V. (b) After the first charge to 4.8 V and then discharged to 3.3 and 2.0 V.

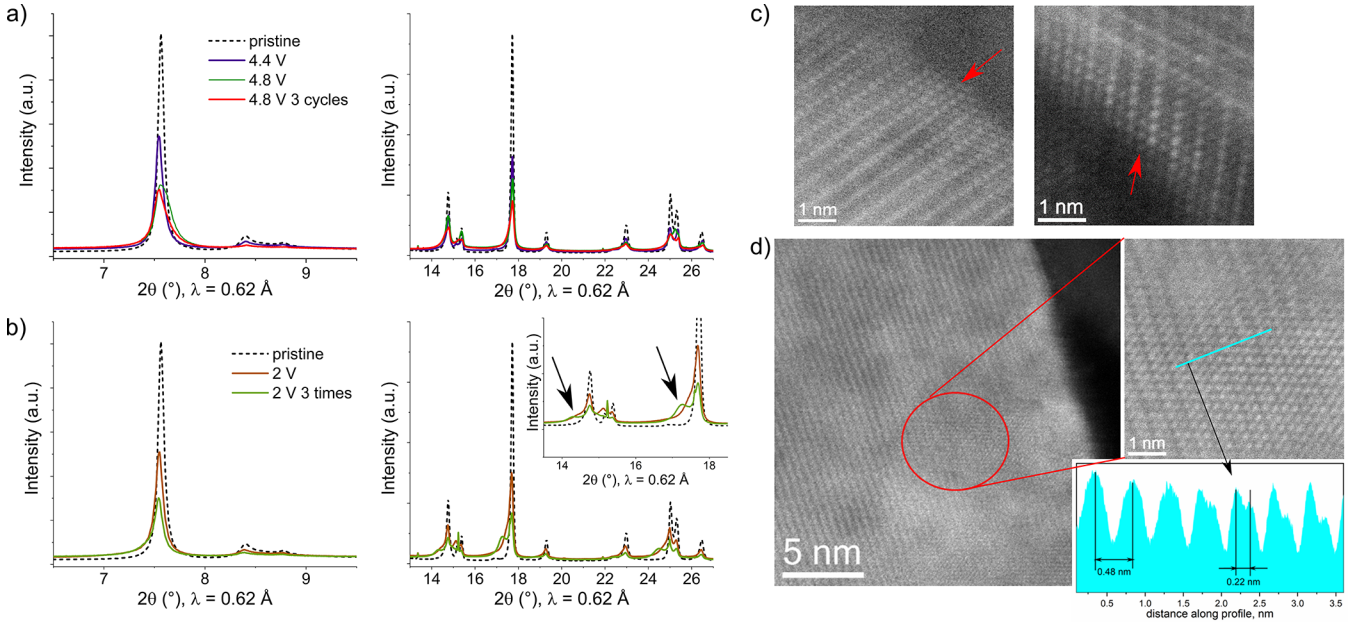

Figure 9. (a and b) Synchrotron XRPD of ex situ samples prepared from Li_2NiO_3 (dis)charged to different voltages. Pristine Li_2NiO_3 is shown as reference as a dashed black line. (a) First charge to 4.4 and 4.8 V and third charge to 4.8 V. (b) Samples recovered after the initial cycle (2.0–4.8 V) in discharged state and after 3 cycles in the same voltage window. (c and d) High resolution HAADF STEM images at different magnifications of the sample after 3 cycles. Rock salt like regions can be observed at the surface (c), as indicated by red arrows, and in the bulk (d) of primary grains. Integrated line profile (light blue) confirms the additional atomic periodicity of the rock salt phase (~1/2 of the pristine monoclinic phase) due to the presence of Ni cations in the positions previously occupied by Li (in the Li layer).

structure of Li_2NiO_3, the question arises as to whether the layered monoclinic structure is at all maintained both after a few cycles and after long term cycling. To verify the stability of the crystal structure after cycling, ex situ samples were prepared as previously described and studied by synchrotron XRPD and TEM. The corresponding results are summarized in Figure 9. During the first charge to 4.8 V, the Bragg reflections change little in position but become broader and less intense (see Figure 9a). The same is observed after the third charge and after the first discharge. However, in the latter case, shoulders are observed on the low angle side of intense Bragg reflections, which transform into clear peaks after the third discharge (marked by arrows in Figure 9b). Their angular positions are close to those one would expect for a cubic rock salt structure, thus indicating that the layered crystal structure is slowly transforming into a rock salt like one during cycling.

These observations are confirmed by operando XRPD of Li_2NiO_3 (see Figure S7), which showed little to no change in the angular positions of the 001_m Bragg reflection, but displayed a progressive intensity loss. The HAADF STEM images gathered in Figure 9c and d give some indication to locate the rock salt domains within the primary grains. In Figure 9c, one can clearly notice surface rock salt regions, which is to be expected from the behavior of most Ni rich CAMs and from the well known instability of their surfaces during cycling.[2,3] Interestingly, rock salt domains could be identified also within the bulk of the primary grains, as shown in Figure 9d. This indicates that the electrochemical cycling of Li_2NiO_3 does not lead to surface degradation as in Ni rich CAMs but instead a more profound degradation of the bulk crystal structure occurs, in agreement with the observation of (i) a large amount of O_2 release from the lattice and (ii) the reflections of a rock salt phase from XRPD (Figure 9b), which is typically a bulk sensitive method.

Furthermore, a Li_2NiO_3 sample was recovered after 100 cycles and studied ex situ to verify the progress of the structural transformation. Figure 10a shows the respective XRPD pattern,

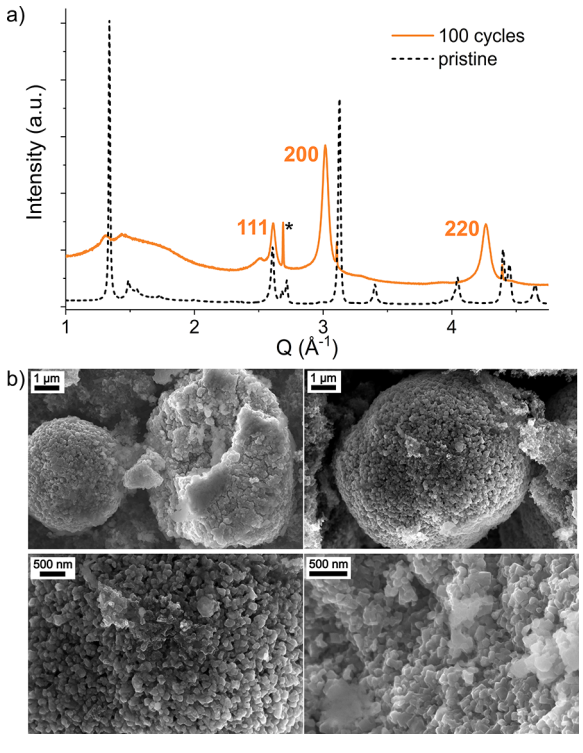

Figure 10. (a) Synchrotron XRPD of an ex situ sample prepared from Li_2NiO_3 after 100 cycles (2.0–4.8 V). Pristine Li_2NiO_3 is shown as reference as a dashed black line. Asterisks indicate reflections from the Al current collector. (b) SEM images at different magnifications of the sample after 100 cycles.

where the intense reflections of the monoclinic structure have disappeared (for example at ~1.4 Å^{-1} in $\vec{q}$ space). Only the reflections related to the rock salt like framework are still observed, albeit rather broad, suggesting complete phase transformation of the lattice. The absence of Bragg reflections of the monoclinic lattice is further confirmed by electron diffraction, as shown in Figure S8. We note that this behavior is markedly different than for layered NCM and even LNO: when these CAMs are extensively cycled (e.g., until they reach only 100 mAh/g_{CAM} residual specific discharge capacity), their bulk crystal structure is still rhombohedral, as observed by XRPD; the rock salt phase these compounds develop is only localized at the surface, and it can only be detected by TEM.[68,85] Furthermore, additional weak Bragg reflections can be noticed by careful inspection of the XRPD pattern background in Figure 10. Although such reflections are too weak and broad to be further analyzed, we show in Figure S9 that their angular position corresponds to the reflections of a layered $LiNiO_2$ like phase, except for a shift indicating a different unit cell volume and hence a different (lower) Li/Ni ratio. This suggests that Li_2NiO_3 decomposes to a rock salt like phase whose cation distribution is not fully randomized, but it still maintains some amount of layering (short to medium range ordering) able to produce the respective broad Bragg reflections.

Rock salt $Li_yNi_{1-y}O$ phases are typically regarded as electrochemically inactive because Li is not diffusing in such dense frameworks. In fact, a Li excess larger than 10% is needed for Li to become mobile in a rock salt phase and hence to make the material electrochemically active.[86] The unit cell volume of the phase shown in Figure 10a is 72.68(3) Å^3, as obtained from Rietveld refinement (see Figure S10 and Table 4). On a volume–composition curve such as that reported in

Table 4. Structural Parameters Obtained from the Rietveld Refinement of the Rock Salt $Li_yNi_{1-y}O$ Phase Shown in Figure 10a[a]

rock salt $Li_yNi_{1-y}O$					XRPD	
S.G.: $Fm\bar{3}m$, $Z = 4$					R_{Bragg} = 7.83%	
a = 4.1708(5) Å					R_{wp} = 16.1%	
V = 72.55(5) Å^3					χ^2 = 4.32	
		atomic position				
atoms	Wyckoff position	x/a	y/b	z/c	Occ	B_{iso}
Ni	4a	0	0	0	0.51(1)	0.75(5)
Li	4a	0	0	0	0.49(1)	0.75(5)
O	4b	0.5	0.5	0.5	1	2.3(2)

[a]The refinement is reported in Figure S10.

ref 2, this large value would correspond to $Li_{0.03}Ni_{0.97}O$, i.e., very little lithiation. This finding conflicts with the low intensity of the 111 reflection I_{111} as compared to that of the 200 reflection, which is a signature of low electronic density on the cation site of the rock salt structure. In fact

$$I_{111} \propto |F_{111}|^2 \propto (f_C - f_A)^2 = (yf_{Li} - (1-y)f_{Ni} - f_O)^2$$

where F_{111} is the structure factor of the 111 reflection and f_C and f_A are form factors of the atoms on the cation and anion sites, respectively. Consequently, a lower value of the form factor f_C, as given, for example, by the high Li content (y) in the cation site, would result in a weak 111 reflection (as simulated in Figure S11). Rietveld refinement indeed yields a composition $Li_{0.49(1)}Ni_{0.51(1)}O$, suggesting a large Li content in the material that might thus lead to sufficient Li mobility. Finally, this also agrees with the fact that after 100 cycles the material is still electrochemically active with a specific capacity of about 100 mAh/g_{CAM}, thereby clearly demonstrating that the rock salt like structure is capable of reversible Li (de)insertion. To estimate the Li diffusivity in such a material, we also carried out a galvanostatic intermittent titration technique (GITT) experiment (Figure S12). We found a Li

diffusivity that varies by around an order of magnitude throughout a full cycle, between 10^{-12} and 10^{-13} cm^2/s. It is expected that the Li diffusivity varies strongly with composition in CAMs and in particular in NCM compounds due to the varying interlayer spacing and/or to the stabilization of given Li/vacancy orderings.[87] In particular, NCM811 has its worst diffusivity at very high and very low Li contents, approximately reaching 10^{-13} and 10^{-12} cm^2/s, respectively; however, for most intermediate compositions, NCM811 has much higher Li diffusivity, approaching 10^{-9} cm^2/s.[88] Hence, we can conclude that our sample exhibits Li diffusivities significantly lower than NCM811 for most Li compositions but comparable to the values obtained at near full lithiation, i.e., still high enough to allow Li (de)insertion at moderate rates.

Figure 10b shows SEM images of the sample after 100 cycles. Although some of the secondary particles appear damaged, it is surprising that the overall morphology is mostly retained. Because mechanical degradation of CAMs is typically a result of large volume changes during cycling, this fact suggests that the electrochemical operation of Li_2NiO_3 does not involve significant volume changes, as corroborated by the ex situ XRPD patterns in Figure 9, showing little change in the angular position of the Bragg reflections. In addition, the high magnification SEM images reveal an increasingly porous microstructure, which presumably results from the large amount of gas released in the initial cycles.

Finally, we attempt to estimate the Li content range of such a compound during cycling. Since the sample was recovered at the bottom of discharge (2 V), the rock salt $Li_{0.49}Ni_{0.51}O$ material mostly cycles in a region with Li/Ni < 1. The specific capacity is 100 mAh/g after 120 cycles, while the theoretical capacity can be estimated as 266.2 mAh/g (assuming a capacity limited by the Li availability of 0.49 Li and a molecular weight of 49.3 g/mol). Hence, about 37% of the available Li is (de)insertion, i.e., the material cycles between $Li_{0.49}Ni_{0.51}O$ and $Li_{0.31}Ni_{0.51}O$ and the average oxidation state varies between 3+ and 3.3+. This also indicates that with the oxygen release in the early cycles, some Li was lost from the cathode (most likely plated on the Li anode). One should note that these values are estimates. The quantifications may be inexact due to the presence of vacancies in the cationic or anionic sites of the rock salt type material, for example, which we have not probed extensively. Vacancies would likely also help improve the Li diffusivity and explain why the material works despite the lack of Li excess, needed for rock salt materials to function in Li ion cells.

Although further investigations are needed regarding the nature and composition of this phase, our observations suggest that it is possible to stabilize (metastable) highly oxidized compounds in the Li−Ni−O space, possessing a disordered cubic rock salt type structure and being capable of Li (de)insertion. Most likely, such phases are not accessible by methods relying on equilibrium thermodynamics such as solid state synthesis but may be accessed by out of equilibrium routes such as ball milling, for example, which is in fact often used to prepare cation disordered rock salt compounds.[80]

CONCLUSIONS AND PERSPECTIVES

In conclusion, we have shown that Li_2NiO_3 and all members of the $Li_{1+x}Ni_{1-x}O_2$ solid solution can be readily prepared by a low temperature solid state synthesis from reactive hydroxide precursors. The crystal structure changes with increasing x values; the hexagonal lattice becomes monoclinic as honeycomb orderings start to evolve within the mixed Li/Ni layer and build a cooperative network. Li_2NiO_3 contains oxygen vacancies, yet the Ni oxidation state is close to tetravalent, as shown by ^{7}Li NMR and by the similarity of soft XAS spectra to those of $Li_{0.1}NiO_2$.

Despite the apparent lack of Ni redox availability, Li_2NiO_3 exhibits a remarkably high first cycle specific charge capacity, which we demonstrate is mostly due to O_2 release from the lattice. However, gas evolution does not account for all of the observed capacity, and we do not find signs of Ni oxidation. Hence, based on the change of the O K edge in soft XAS, we suggest that reversible O redox activity might be present. After the first cycle and the significant change in composition due to oxygen loss, the material continues to present electrochemical activity with a specific capacity stabilizing at about 100 mAh/g_{CAM} after 120 cycles (likely due to standard redox mechanisms). Although such results can surely be improved by optimization of the material, the lessons learned on $LiNiO_2$ suggest it is unlikely that a cathode based on highly oxidized Ni can be fully stabilized. On the other hand, Li_2NiO_3 can act as a new end member, extending the compositional space available for exploration of new CAMs based on $LiMO_2$ and Li_2MO_3.

Furthermore, we highlight how the first few cycles induce irreversible structural changes in the material, which result in complete loss of Bragg reflections of the monoclinic lattice in favor of a rock salt like lattice. On the basis of the residual redox activity and analysis of the diffraction patterns after ∼100 cycles, we conclude that the stabilized phase is a disordered rock salt material with a large Li/Ni ratio, displaying lithium mobility and hence electrochemical activity, never reported to date. In this respect, we suggest that metastable disordered rock salt materials can be stabilized in the Li−Ni−O space, likely by non thermodynamic synthesis routes and without the need for other high valence cations.[25,89] Our study demonstrates that new compounds with exciting properties may still be discovered in the area of Li rich Ni based oxides.

AUTHOR INFORMATION

Corresponding Author

Matteo Bianchini − *Battery and Electrochemistry Laboratory, Institute of Nanotechnology, Karlsruhe Institute of Technology (KIT), 76344 Eggenstein Leopoldshafen, Germany; BASF SE,*

67056 Ludwigshafen, Germany; orcid.org/0000 0003 4034 7706; Email: matteo.bianchini@kit.edu

Authors

Alexander Schiele – *Battery and Electrochemistry Laboratory, Institute of Nanotechnology, Karlsruhe Institute of Technology (KIT), 76344 Eggenstein Leopoldshafen, Germany*

Simon Schweidler – *Battery and Electrochemistry Laboratory, Institute of Nanotechnology, Karlsruhe Institute of Technology (KIT), 76344 Eggenstein Leopoldshafen, Germany*

Sabrina Sicolo – *BASF SE, 67056 Ludwigshafen, Germany;* orcid.org/0000 0001 8575 3834

François Fauth – *CELLS–ALBA Synchrotron, 08290 Barcelona, Spain;* orcid.org/0000 0001 9465 3106

Emmanuelle Suard – *Institut Laue Langevin, 38042 Grenoble Cedex 9, France;* orcid.org/0000 0001 5966 5929

Sylvio Indris – *Institute for Applied Materials, Karlsruhe Institute of Technology (KIT), 76344 Eggenstein Leopoldshafen, Germany;* orcid.org/0000 0002 5100 113X

Andrey Mazilkin – *Battery and Electrochemistry Laboratory, Institute of Nanotechnology, Karlsruhe Institute of Technology (KIT), 76344 Eggenstein Leopoldshafen, Germany; Institute of Solid State Physics, Russian Academy of Sciences, 142432 Chernogolovka, Russia*

Peter Nagel – *Institute for Quantum Materials and Technologies, Karlsruhe Institute of Technology (KIT), 76021 Karlsruhe, Germany*

Stefan Schuppler – *Institute for Quantum Materials and Technologies, Karlsruhe Institute of Technology (KIT), 76021 Karlsruhe, Germany*

Michael Merz – *Institute for Quantum Materials and Technologies, Karlsruhe Institute of Technology (KIT), 76021 Karlsruhe, Germany*

Pascal Hartmann – *Battery and Electrochemistry Laboratory, Institute of Nanotechnology, Karlsruhe Institute of Technology (KIT), 76344 Eggenstein Leopoldshafen, Germany; BASF SE, 67056 Ludwigshafen, Germany*

Torsten Brezesinski – *Battery and Electrochemistry Laboratory, Institute of Nanotechnology, Karlsruhe Institute of Technology (KIT), 76344 Eggenstein Leopoldshafen, Germany;* orcid.org/0000 0002 4336 263X

Jürgen Janek – *Battery and Electrochemistry Laboratory, Institute of Nanotechnology, Karlsruhe Institute of Technology (KIT), 76344 Eggenstein Leopoldshafen, Germany; Institute of Physical Chemistry & Center for Materials Science (ZfM/LaMa), Justus Liebig University Giessen, 35392 Giessen, Germany;* orcid.org/0000 0002 9221 4756

Complete contact information is available at: https://pubs.acs.org/10.1021/acs.chemmater.0c02880

Notes

The authors declare no competing financial interest.

■ ACKNOWLEDGMENTS

This study was part of the projects being funded by BASF SE. We thank Dr. Thomas Bergfeldt for ICP OES measurements. The authors acknowledge MSPD and the ALBA synchrotron for the beamtime awarded under proposal 2018093026. We acknowledge the synchrotron light source KARA for the provision of beamtime and the KNMF (Karlsruhe, Germany) for access to its facilities. We thank Holger Geßwein for support with operando XRPD measurements and Raffael Rueß for support and discussion with electrochemical measurements.

■ REFERENCES

(1) Blomgren, G. E. The Development and Future of Lithium Ion Batteries. *J. Electrochem. Soc.* **2017**, *164* (1), A5019–A5025.

(2) Bianchini, M.; Roca Ayats, M.; Hartmann, P.; Brezesinski, T.; Janek, J. There and Back Again The Journey of LiNiO2 as a Cathode Active Material. *Angew. Chem., Int. Ed.* **2019**, *58*, 10434–10458.

(3) Xu, J.; Lin, F.; Doeff, M. M.; Tong, W. A review of Ni based layered oxides for rechargeable Li ion batteries. *J. Mater. Chem. A* **2017**, *5* (3), 874–901.

(4) Li, W.; Erickson, E. M.; Manthiram, A. High nickel layered oxide cathodes for lithium based automotive batteries. *Nat. Energy* **2020**, *5* (1), 26–34.

(5) Bronger, W.; Bade, H.; Klemm, W. Zur Kenntnis Der Niccolate Der Alkalimetalle. *Z. Anorg. Allg. Chem.* **1964**, *333* (4–6), 188–200.

(6) Goodenough, J. B.; Wickham, D. G.; Croft, W. J. Some Magnetic and Crystallographic Properties of the System $Li_x^{+}Ni_{1-2x}^{+2}Ni_x^{+++}O$. *J. Phys. Chem. Solids* **1958**, *5* (1–2), 107–116.

(7) Goodenough, J. B.; Wickham, D. G.; Croft, W. J. Some Ferrimagnetic Properties of the System LixNi1–xO. *J. Appl. Phys.* **1958**, *29* (3), 382–383.

(8) Moore, R. J.; White, J. Equilibrium Relationships in Systems Li Co O and Li Ni O. *J. Mater. Sci.* **1974**, *9* (9), 1401–1408.

(9) Migeon, H. N.; Zanne, M.; Gleitzer, C.; Aubry, J. Li2O NiO O2 System at 670 Degrees C and Consequences of Nonstoichiometry on Magnetic Properties of Lixni1 Xo1+Y Phases. *J. Mater. Sci.* **1978**, *13* (3), 461–466.

(10) Berbenni, V.; Massarotti, V.; Capsoni, D.; Riccardi, R.; Marini, A.; Antolini, E. Structural and Microstructural Study of the Formation of the Solid Solution Lixni1 Xo. *Solid State Ionics* **1991**, *48* (1–2), 101–111.

(11) Antolini, E. LixNi1–xO ($0<x \leq 0.3$) solid solutions: formation, structure and transport properties. *Mater. Chem. Phys.* **2003**, *82* (3), 937–948.

(12) Jansen, M.; Hoppe, R. Zur Kenntnis der NaCl Strukturfamilie: Neue Untersuchungen an Li2MnO3. *Z. Anorg. Allg. Chem.* **1973**, *397* (3), 279–289.

(13) Migeon, H.; Courtois, A.; Zanne, M.; Gleitzer, C. Preparation and Study of Li_2NiO_{3-y} (*y* less than or equal to 0.135). *Rev. Chim. Minér.* **1976**, *13* (1), 1–8.

(14) Stoyanova, R.; Zhecheva, E.; Alcántara, R.; Tirado, J. L.; Bromiley, G.; Bromiley, F.; Boffa Ballaran, T. Lithium/nickel mixing in the transition metal layers of lithium nickelate: high pressure synthesis of layered Li[LixNi1–x]O2 oxides as cathode materials for lithium ion batteries. *Solid State Ionics* **2003**, *161* (3), 197–204.

(15) Shinova, E.; Zhecheva, E.; Stoyanova, R.; Bromiley, G. D. High pressure synthesis of solid solutions between trigonal LiNiO2 and monoclinic Li[Li1/3Ni2/3]O2. *J. Solid State Chem.* **2005**, *178* (5), 1661–1669.

(16) Tabuchi, M.; Kuriyama, N.; Takamori, K.; Imanari, Y.; Nakane, K. Appearance of Lithium Excess LiNiO2with High Cyclability Synthesized by Thermal Decomposition Route from LiNiO2 Li2NiO3Solid Solution. *J. Electrochem. Soc.* **2016**, *163* (10), A2312–A2317.

(17) Kobayashi, Y.; Tabuchi, M.; Miyashiro, H.; Kuriyama, N. A new design of highly reversible LiNiO 2: Defect formation in transition metal site. *J. Power Sources* **2017**, *364*, 156–162.

(18) Gottschall, R.; Schöllhorn, R.; Muhler, M.; Jansen, N.; Walcher, D.; Gütlich, P. Electronic State of Nickel in Barium Nickel Oxide, BaNiO3. *Inorg. Chem.* **1998**, *37* (7), 1513–1518.

(19) Lacorre, P.; Torrance, J. B.; Pannetier, J.; Nazzal, A. I.; Wang, P. W.; Huang, T. C. Synthesis, Crystal Structure, and Properties of Metallic Prnio3 Comparison with Metallic Ndnio3 and Semi conducting Smnio3. *J. Solid State Chem.* **1991**, *91* (2), 225–237.

(20) Mizokawa, T.; Fujimori, A.; Arima, T.; Tokura, Y.; Mori, N.; Akimitsu, J. Electronic Structure of Prnio3 Studied by Photoemission and X Ray Absorption Spectroscopy Band Gap and Orbital Ordering. *Phys. Rev. B: Condens. Matter Mater. Phys.* **1995**, *52* (19), 13865–13873.

(21) Mansour, A. N.; Melendres, C. A.; Pankuch, M.; Brizzolara, R. A. X Ray Absorption Fine Structure Spectra and the Oxidation State of Nickel in Some of Its Oxycompounds. *J. Electrochem. Soc.* **1994**, *141* (6), L69−L71.
(22) Koga, H.; Croguennec, L.; Mannessiez, P.; Menetrier, M.; Weill, F.; Bourgeois, L.; Duttine, M.; Suard, E.; Delmas, C. Li1.20Mn0.54Co0.13Ni0.13O2 with Different Particle Sizes as Attractive Positive Electrode Materials for Lithium Ion Batteries: Insights into Their Structure. *J. Phys. Chem. C* **2012**, *116* (25), 13497−13506.
(23) Luo, K.; Roberts, M. R.; Hao, R.; Guerrini, N.; Pickup, D. M.; Liu, Y. S.; Edstrom, K.; Guo, J. H.; Chadwick, A. V.; Duda, L. C.; Bruce, P. G. Charge compensation in 3d transition metal oxide intercalation cathodes through the generation of localized electron holes on oxygen. *Nat. Chem.* **2016**, *8* (7), 684−691.
(24) Lu, Z. H.; MacNeil, D. D.; Dahn, J. R. Layered cathode materials Li NixLi(1/3−2x/3)Mn(2/3 x/3) O 2 for lithium ion batteries. *Electrochem. Solid State Lett.* **2001**, *4* (11), A191−A194.
(25) Kim, S.; Aykol, M.; Hegde, V. I.; Lu, Z.; Kirklin, S.; Croy, J. R.; Thackeray, M. M.; Wolverton, C. Material design of high capacity Li rich layered oxide electrodes: Li2MnO3 and beyond. *Energy Environ. Sci.* **2017**, *10* (10), 2201−2211.
(26) Rozier, P.; Tarascon, J. M. Review—Li Rich Layered Oxide Cathodes for Next Generation Li Ion Batteries: Chances and Challenges. *J. Electrochem. Soc.* **2015**, *162* (14), A2490−A2499.
(27) Croy, J. R.; Balasubramanian, M.; Gallagher, K. G.; Burrell, A. K. Review of the U.S. Department of Energy's "Deep Dive" Effort to Understand Voltage Fade in Li and Mn Rich Cathodes. *Acc. Chem. Res.* **2015**, *48* (11), 2813−2821.
(28) Shao Horn, Y.; Ein Eli, Y.; Robertson, A. D.; Averill, W. F.; Hackney, S. A.; Howard, W. F. Morphology Modification and Delithiation Mechanisms of LiMn2O4 and Li2MnO3 by Acid Digestion. *J. Electrochem. Soc.* **1998**, *145* (1), 16.
(29) Johnson, C. S.; Korte, S. D.; Vaughey, J. T.; Thackeray, M. M.; Bofinger, T. E.; Shao Horn, Y.; Hackney, S. A. Structural and electrochemical analysis of layered compounds from Li2MnO3. *J. Power Sources* **1999**, *81−82*, 491−495.
(30) Kalyani, P.; Chitra, S.; Mohan, T.; Gopukumar, S. Lithium metal rechargeable cells using Li2MnO3 as the positive electrode. *J. Power Sources* **1999**, *80* (1), 103−106.
(31) Robertson, A. D.; Bruce, P. G. Mechanism of Electrochemical Activity in Li2MnO3. *Chem. Mater.* **2003**, *15* (10), 1984−1992.
(32) Croy, J. R.; Park, J. S.; Dogan, F.; Johnson, C. S.; Key, B.; Balasubramanian, M. First Cycle Evolution of Local Structure in Electrochemically Activated Li2MnO3. *Chem. Mater.* **2014**, *26* (24), 7091−7098.
(33) Rana, J.; Papp, J. K.; Lebens Higgins, Z.; Zuba, M.; Kaufman, L. A.; Goel, A.; Schmuch, R.; Winter, M.; Whittingham, M. S.; Yang, W.; McCloskey, B. D.; Piper, L. F. J. Quantifying the Capacity Contributions during Activation of Li2MnO3. *ACS Energy Letters* **2020**, *5* (2), 634−641.
(34) Lee, E.; Persson, K. A. Structural and Chemical Evolution of the Layered Li Excess LixMnO3 as a Function of Li Content from First Principles Calculations. *Adv. Energy Mater.* **2014**, *4* (15), 1400498.
(35) Yan, P. F.; Xiao, L.; Zheng, J. M.; Zhou, Y. G.; He, Y.; Zu, X. T.; Mao, S. X.; Xiao, J.; Gao, F.; Zhang, J. G.; Wang, C. M. Probing the Degradation Mechanism of Li2MnO3 Cathode for Li Ion Batteries. *Chem. Mater.* **2015**, *27* (3), 975−982.
(36) Fauth, F.; Peral, I.; Popescu, C.; Knapp, M. The new Material Science Powder Diffraction beamline at ALBA Synchrotron. *Powder Diffr.* **2013**, *28* (S2), S360−S370.
(37) Rietveld, H. M. A profile refinement method for nuclear and magnetic structures. *J. Appl. Crystallogr.* **1969**, *2*, 65.
(38) Rodriguez Carvajal, J. Recent advances in magnetic structure determination by neutron powder diffraction. *Phys. B* **1993**, *192* (1−2), 55−69.
(39) Casas Cabanas, M.; Reynaud, M.; Rikarte, J.; Horbach, P.; Rodriguez Carvajal, J. FAULTS: a program for refinement of structures with extended defects. *J. Appl. Crystallogr.* **2016**, *49* (6), 2259−2269.
(40) Merz, M.; Fuchs, D.; Assmann, A.; Uebe, S.; von Lohneysen, H.; Nagel, P.; Schuppler, S. Spin and orbital states in single layered La2 xCaxCoO4 studied by doping and temperature dependent near edge x ray absorption fine structure. *Phys. Rev. B: Condens. Matter Mater. Phys.* **2011**, *84* (1), 014436.
(41) Merz, M.; Nagel, P.; Pinta, C.; Samartsev, A.; von Lohneysen, H.; Wissinger, M.; Uebe, S.; Assmann, A.; Fuchs, D.; Schuppler, S. X ray absorption and magnetic circular dichroism of LaCoO3, La0.7Ce0.3CoO3, and La0.7Sr0.3CoO3 films: Evidence for cobalt valence dependent magnetism. *Phys. Rev. B: Condens. Matter Mater. Phys.* **2010**, *82* (17), 174416.
(42) Berkes, B. B.; Schiele, A.; Sommer, H.; Brezesinski, T.; Janek, J. On the gassing behavior of lithium ion batteries with NCM523 cathodes. *J. Solid State Electrochem.* **2016**, *20* (11), 2961−2967.
(43) Schiele, A.; Hatsukade, T.; Berkes, B. B.; Hartmann, P.; Brezesinski, T.; Janek, J. High Throughput in Situ Pressure Analysis of Lithium Ion Batteries. *Anal. Chem.* **2017**, *89* (15), 8122−8128.
(44) Berkes, B. B.; Jozwiuk, A.; Sommer, H.; Brezesinski, T.; Janek, J. Simultaneous acquisition of differential electrochemical mass spectrometry and infrared spectroscopy data for in situ character ization of gas evolution reactions in lithium ion batteries. *Electrochem. Commun.* **2015**, *60*, 64−69.
(45) Berkes, B. B.; Jozwiuk, A.; Vracar, M.; Sommer, H.; Brezesinski, T.; Janek, J. Online Continuous Flow Differential Electrochemical Mass Spectrometry with a Realistic Battery Setup for High Precision, Long Term Cycling Tests. *Anal. Chem.* **2015**, *87* (12), 5878−5883.
(46) Kresse, G.; Furthmüller, J. Efficiency of ab initio total energy calculations for metals and semiconductors using a plane wave basis set. *Comput. Mater. Sci.* **1996**, *6* (1), 15−50.
(47) Kresse, G.; Furthmuller, J. Efficient iterative schemes for ab initio total energy calculations using a plane wave basis set. *Phys. Rev. B: Condens. Matter Mater. Phys.* **1996**, *54* (16), 11169−11169.
(48) Blöchl, P. E. Projector augmented wave method. *Phys. Rev. B: Condens. Matter Mater. Phys.* **1994**, *50* (24), 17953−17979.
(49) Kresse, G.; Joubert, D. From ultrasoft pseudopotentials to the projector augmented wave method. *Phys. Rev. B: Condens. Matter Mater. Phys.* **1999**, *59* (3), 1758.
(50) Peng, H. W.; Yang, Z. H.; Perdew, J. P.; Sun, J. W. Versatile van der Waals Density Functional Based on a Meta Generalized Gradient Approximation. *Phys. Rev. X* **2016**, *6* (4), 041005.
(51) Okhotnikov, K.; Charpentier, T.; Cadars, S. Supercell program: a combinatorial structure generation approach for the local level modeling of atomic substitutions and partial occupancies in crystals. *J. Cheminf.* **2016**, *8*, 17.
(52) Ong, S. P.; Wang, L.; Kang, B.; Ceder, G. Li Fe P O 2 phase diagram from first principles calculations. *Chem. Mater.* **2008**, *20* (5), 1798−1807.
(53) Strobel, P.; Lambert Andron, B. Crystallographic and magnetic structure of Li2MnO3. *J. Solid State Chem.* **1988**, *75* (1), 90−98.
(54) Liu, H.; Liu, H.; Lapidus, S. H.; Meng, Y. S.; Chupas, P. J.; Chapman, K. W. Sensitivity and Limitations of Structures from X ray and Neutron Based Diffraction Analyses of Transition Metal Oxide Lithium Battery Electrodes. *J. Electrochem. Soc.* **2017**, *164* (9), A1802−A1811.
(55) Bianchini, M.; Fauth, F.; Hartmann, P.; Brezesinski, T.; Janek, J. An in situ structural study on the synthesis and decomposition of LiNiO2. *J. Mater. Chem. A* **2020**, *8* (4), 1808−1820.
(56) Biscoe, J.; Warren, B. E. An X Ray Study of Carbon Black. *J. Appl. Phys.* **1942**, *13* (6), 364−371.
(57) Serrano Sevillano, J.; Carlier, D.; Saracibar, A.; Lopez del Amo, J. M.; Casas Cabanas, M. Lopez del Amo, J. M.; Casas Cabanas, M., DFT Assisted Solid State NMR Characterization of Defects in Li2MnO3. *Inorg. Chem.* **2019**, *58* (13), 8347−8356.
(58) Casas Cabanas, M.; Rodríguez Carvajal, J.; Canales Vázquez, J.; Laligant, Y.; Lacorre, P.; Palacín, M. R. Microstructural character isation of battery materials using powder diffraction data: DIFFaX,

FAULTS and SH FullProf approaches. *J. Power Sources* **2007**, *174* (2), 414−420.
(59) Yu, D. Y. W.; Yanagida, K.; Kato, Y.; Nakamura, H. Electrochemical Activities in Li2MnO3. *J. Electrochem. Soc.* **2009**, *156* (6), A417−A424.
(60) Boulineau, A.; Croguennec, L.; Delmas, C.; Weill, F. Reinvestigation of Li2MnO3 Structure: Electron Diffraction and High Resolution TEM. *Chem. Mater.* **2009**, *21* (18), 4216−4222.
(61) Boulineau, A.; Croguennec, L.; Delmas, C.; Weill, F. Structure of Li2MnO3 with different degrees of defects. *Solid State Ionics* **2010**, *180* (40), 1652−1659.
(62) Serrano Sevillano, J.; Reynaud, M.; Saracibar, A.; Altantzis, T.; Bals, S.; van Tendeloo, G.; Casas Cabanas, M. Enhanced electro chemical performance of Li rich cathode materials through micro structural control. *Phys. Chem. Chem. Phys.* **2018**, *20* (35), 23112−23122.
(63) Bareño, J.; Lei, C. H.; Wen, J. G.; Kang, S. H.; Petrov, I.; Abraham, D. P. Local Structure of Layered Oxide Electrode Materials for Lithium Ion Batteries. *Adv. Mater.* **2010**, *22* (10), 1122−1127.
(64) Menon, A. S.; Ojwang, D. O.; Willhammar, T.; Peterson, V. K.; Edström, K.; Gomez, C. P.; Brant, W. R. Influence of Synthesis Routes on the Crystallography, Morphology, and Electrochemistry of Li2MnO3. *ACS Appl. Mater. Interfaces* **2020**, *12* (5), 5939−5950.
(65) Shannon, R. Revised effective ionic radii and systematic studies of interatomic distances in halides and chalcogenides. *Acta Crystallogr., Sect. A: Cryst. Phys., Diffr., Theor. Gen. Crystallogr.* **1976**, *32* (5), 751−767.
(66) Aydinol, M. K.; Kohan, A. F.; Ceder, G.; Cho, K.; Joannopoulos, J. Ab initio study of lithium intercalation in metal oxides and metal dichalcogenides. *Phys. Rev. B: Condens. Matter Mater. Phys.* **1997**, *56* (3), 1354−1365.
(67) Kong, F.; Liang, C.; Wang, L.; Zheng, Y.; Perananthan, S.; Longo, R. C.; Ferraris, J. P.; Kim, M.; Cho, K. Kinetic Stability of Bulk LiNiO2 and Surface Degradation by Oxygen Evolution in LiNiO2 Based Cathode Materials. *Adv. Energy Mater.* **2019**, *9* (2), 1802586.
(68) Xu, J.; Hu, E.; Nordlund, D.; Mehta, A.; Ehrlich, S. N.; Yang, X. Q.; Tong, W. Understanding the Degradation Mechanism of Lithium Nickel Oxide Cathodes for Li Ion Batteries. *ACS Appl. Mater. Interfaces* **2016**, *8* (46), 31677−31683.
(69) Xu, J.; Lin, F.; Nordlund, D.; Crumlin, E. J.; Wang, F.; Bai, J.; Doeff, M. M.; Tong, W. Elucidation of the surface characteristics and electrochemistry of high performance LiNiO2. *Chem. Commun. (Cambridge, U. K.)* **2016**, *52* (22), 4239−42.
(70) Yoon, W. S.; Balasubramanian, M.; Chung, K. Y.; Yang, X. Q.; McBreen, J.; Grey, C. P.; Fischer, D. A. Investigation of the Charge Compensation Mechanism on the Electrochemically Li Ion Dein tercalated Li1 xCo1/3Ni1/3Mn1/3O2 Electrode System by Combi nation of Soft and Hard X ray Absorption Spectroscopy. *J. Am. Chem. Soc.* **2005**, *127* (49), 17479−17487.
(71) Yoon, W. S.; Chung, K. Y.; McBreen, J.; Fischer, D. A.; Yang, X. Q. Changes in electronic structure of the electrochemically Li ion deintercalated LiNiO2 system investigated by soft X ray absorption spectroscopy. *J. Power Sources* **2006**, *163* (1), 234−237.
(72) Ikeno, H.; de Groot, F. M. F.; Stavitski, E.; Tanaka, I. Multiplet calculations of L2,3x ray absorption near edge structures for 3d transition metal compounds. *J. Phys.: Condens. Matter* **2009**, *21* (10), 104208.
(73) Kleiner, K.; Murray, C.; Grosu, C.; Day, S.; Winter, M.; Nagel, P.; Schuppler, S.; Merz, M. On the microscopic origin of reversible and irreversible reactions of LiNixCoyMnx cathode materials: Ni O hybrid bond formation vs. cationic and anionic redox. ArXiv.org **2020** https://arxiv.org/abs/2006.09964 (accessed on 9−9−2020).
(74) Kuiper, P.; Kruizinga, G.; Ghijsen, J.; Sawatzky, G. A.; Verweij, H. Character of Holes in LixNi1 xO and Their Magnetic Behavior. *Phys. Rev. Lett.* **1989**, *62* (2), 221−224.
(75) van Elp, J.; Searle, B. G.; Sawatzky, G. A.; Sacchi, M. Ligand hole induced symmetry mixing of d8 states in LixNi1−xO, as observed in Ni 2p x ray absorption spectroscopy. *Solid State Commun.* **1991**, *80* (1), 67−71.
(76) Chen, H.; Freeman, C. L.; Harding, J. H. Charge disproportionation and Jahn Teller distortion in LiNiO2and NaNiO2: A density functional theory study. *Phys. Rev. B: Condens. Matter Mater. Phys.* **2011**, *84* (8), 085108.
(77) Grey, C. P.; Dupre, N. NMR studies of cathode materials for lithium ion rechargeable batteries. *Chem. Rev.* **2004**, *104* (10), 4493−4512.
(78) Carlier, D.; Ménétrier, M.; Grey, C. P.; Delmas, C.; Ceder, G. Understanding the NMR shifts in paramagnetic transition metal oxides using density functional theory calculations. *Phys. Rev. B: Condens. Matter Mater. Phys.* **2003**, *67* (17), 174103.
(79) Marker, K.; Reeves, P. J.; Xu, C.; Griffith, K. J.; Grey, C. P. Evolution of Structure and Lithium Dynamics in LiNi0.8Mn0.1 Co0.1O2 (NMC811) Cathodes during Electrochemical Cycling. *Chem. Mater.* **2019**, *31* (7), 2545−2554.
(80) Clement, R. J.; Lun, Z.; Ceder, G. Cation disordered rocksalt transition metal oxides and oxyfluorides for high energy lithium ion cathodes. *Energy Environ. Sci.* **2020**, *13* (2), 345−373.
(81) de Biasi, L.; Schiele, A.; Roca Ayats, M.; Garcia, G.; Brezesinski, T.; Hartmann, P.; Janek, J. Phase Transformation Behavior and Stability of LiNiO2 Cathode Material for Li Ion Batteries Obtained from In Situ Gas Analysis and Operando X Ray Diffraction. *ChemSusChem* **2019**, *12* (10), 2240−2250.
(82) Hatsukade, T.; Schiele, A.; Hartmann, P.; Brezesinski, T.; Janek, J. Origin of Carbon Dioxide Evolved during Cycling of Nickel Rich Layered NCM Cathodes. *ACS Appl. Mater. Interfaces* **2018**, *10* (45), 38892−38899.
(83) Li, N.; Sallis, S.; Papp, J. K.; Wei, J.; Mccloskey, B.; Yang, W. L.; Tong, W. Unraveling the Cationic and Anionic Redox Reactions in a Conventional Layered Oxide Cathode. *Acs Energy Letters* **2019**, *4* (12), 2836−2842.
(84) Teufl, T.; Strehle, B.; Muller, P.; Gasteiger, H. A.; Mendez, M. A. Oxygen Release and Surface Degradation of Li and Mn Rich Layered Oxides in Variation of the Li2MnO3 Content. *J. Electrochem. Soc.* **2018**, *165* (11), A2718−A2731.
(85) Schweidler, S.; de Biasi, L.; Garcia, G.; Mazilkin, A.; Hartmann, P.; Brezesinski, T.; Janek, J. Investigation into Mechanical Degradation and Fatigue of High Ni NCM Cathode Material: A Long Term Cycling Study of Full Cells. *ACS Appl. Energy Mater.* **2019**, *2* (10), 7375−7384.
(86) Urban, A.; Lee, J.; Ceder, G. The Configurational Space of Rocksalt Type Oxides for High Capacity Lithium Battery Electrodes. *Adv. Energy Mater.* **2014**, *4* (13), 1400478.
(87) Van der Ven, A.; Ceder, G. Lithium Diffusion in Layered Li x CoO2. *Electrochem. Solid State Lett.* **1999**, *3* (7), 301−304.
(88) Ruess, R.; Schweidler, S.; Hemmelmann, H.; Conforto, G.; Bielefeld, A.; Weber, D. A.; Sann, J.; Elm, M. T.; Janek, J. Influence of NCM Particle Cracking on Kinetics of Lithium Ion Batteries with Liquid or Solid Electrolyte. *J. Electrochem. Soc.* **2020**, *167* (10), 100532.
(89) Ji, H.; Kitchaev, D. A.; Lun, Z.; Kim, H.; Foley, E.; Kwon, D. H.; Tian, Y.; Balasubramanian, M.; Bianchini, M.; Cai, Z.; Clément, R. J.; Kim, J. C.; Ceder, G. Computational Investigation and Experimental Realization of Disordered High Capacity Li Ion Cathodes Based on Ni Redox. *Chem. Mater.* **2019**, *31* (7), 2431−2442.